The Astrophysical Journal, 868:10 (26pp), 2018 November 20 https://doi.org/10.3847/1538-4357/aae390

A Study of X-Ray Emission of Galaxies Hosting Molecular Outflows (MOX Sample)

Sibasish Laha[1], Matteo Guainazzi[2], Enrico Piconcelli[3], Poshak Gandhi[4], Claudio Ricci[5,6,7], Ritesh Ghosh[8], Alex G. Markowitz[1,9], and Joydeep Bagchi[10]

[1] University of California, San Diego, Center for Astrophysics and Space Sciences, 9500 Gilman Dr., La Jolla, CA 92093-0424, USA; slaha@ucsd.edu, sib.laha@gmail.com
[2] European Space Research and Technology Centre, Keplerlaan 1, 2201 AZ Noordwijk, The Netherlands
[3] Observatorio Astronomico di Roma (INAF), via Frascati 33, I-00040, Monte Porzio Catone, Roma, Italy
[4] Department of Physics and Astronomy, University of Southampton, Highfield, Southampton SO17 1BJ, UK
[5] Núcleo de Astronomía de la Facultad de Ingeniería, Universidad Diego Portales, Av. Ejército Libertador 441, Santiago, Chile
[6] Kavli Institute for Astronomy and Astrophysics, Peking University, Beijing 100871, People's Republic of China
[7] Chinese Academy of Sciences South America Center for Astronomy, Camino El Observatorio 1515, Las Condes, Santiago, Chile
[8] Visva-Bharati University, Santiniketan, Bolpur 731235, West Bengal, India
[9] Nicolaus Copernicus Astronomical Center, Polish Academy of Sciences, Bartycka 18, PL-00-716 Warszawa, Poland
[10] Inter University Centre for Astronomy and Astrophysics, Post Bag 4, Ganeshkhind, Pune, India
Received 2018 February 15; revised 2018 September 13; accepted 2018 September 20; published 2018 November 13

Abstract

We have carried out an extensive X-ray spectral analysis of a sample of galaxies exhibiting molecular outflows (MOX sample) to characterize the X-ray properties and investigate the effect of active galactic nuclei (AGNs) on the dynamical properties of the molecular outflows (MOs). We find that the X-ray bolometric correction ($L_{2-10\,\mathrm{keV}}/L_{\mathrm{AGN}}$) of these sources ranges from $\sim 10^{-4.5}$ to $10^{-0.5}$, with $\sim$70% of the sources below 10^{-2}, implying a weak X-ray emission relative to the AGN bolometric luminosity (L_{AGN}). However, the upper limit on the 2–10 keV luminosity ($L_{2-10\ \mathrm{keV},\ 12\,\mu\mathrm{m}}$) obtained from 12 μm flux, following the correlation derived by Asmus et al., is $\sim$0.5–3 orders of magnitude larger than the $L_{2-10\,\mathrm{keV}}$ values estimated using X-ray spectroscopy, implying a possibility that the MOX sources host normal AGNs (not X-ray weak), and their X-ray spectra are extremely obscured. We find that both $L_{2-10\,\mathrm{keV}}$ and L_{AGN} correlate strongly with the MO velocity and the mass outflow rates ($\dot{M}_{\mathrm{out}}$), implying that the central AGN plays an important role in driving these massive outflows. However, we also find statistically significant positive correlations between the starburst emission and MO mass outflow rate, $L_{\mathrm{Starburst}}$ versus $\dot{M}_{\mathrm{out}}$, and $L_{0.6-2\mathrm{keV}}$ versus $\dot{M}_{\mathrm{out}}$, which implies that starbursts can generate and drive the MOs. The correlations of MO velocity and $\dot{M}_{\mathrm{out}}$ with AGN luminosities are found to be stronger compared to those with the starburst luminosities. We conclude that both starbursts and AGNs play a crucial role in driving the large-scale MO.

Key words: galaxies: active – galaxies: starburst – ISM: jets and outflows – ISM: molecules – X-rays: galaxies

1. Introduction

The tight correlation between the mass of the central super massive black hole (SMBH) and the stellar bulge velocity distribution points to a coevolution of a black hole and its host galaxy over cosmological times (Ferrarese & Merritt 2000; Gebhardt et al. 2000). However, the exact nature of the interaction is still not clearly understood. Energetic outflows detected in absorption and emission in different wavelength bands have been postulated to be important mechanisms responsible for galaxy SMBH coevolution (see, e.g., Fabian 2012, and references therein).

With the advent of high spatial resolution IR and radio telescopes in the past couple of decades, we have made rapid progress in understanding the nature of the molecular outflows (MOs), which are outflows detected using the broad CO (*I–J*) emission lines, OH absorption lines, HCN and SiO emission lines, and several other molecular tracers (Sturm et al. 2011; Aalto et al. 2012; Veilleux et al. 2013; Brusa et al. 2015, 2018; Feruglio et al. 2015; Stone et al. 2016). In several cases where the host galaxies can be spatially resolved, the outflows have been found to extend to a few kiloparsecs, and these are believed to be one of the most powerful mechanisms by which the SMBH deposits matter onto its host galaxy. The relation between SMBHs and MOs, as well as the mechanism through which MOs would interact with and deposit energy into the interstellar medium (ISM), is still poorly understood.

The effect of the central active galactic nucleus (AGN) on the kiloparsec-scale MO is still debated. Several investigations (see, e.g., Sturm et al. 2011; Veilleux et al. 2013; Cicone et al. 2014) have revealed that the presence of an AGN in the host galaxy boosts the power of the MO. However, we still do not have a consensus on how the AGN interacts with the host galaxy molecular clouds and drives the outflows at kiloparsec scales. Tombesi et al. (2015) and Feruglio et al. (2015) have suggested that the ultrafast outflows (UFOs) detected in X-rays may interact with the ISM of the host galaxy and generate MOs in an energy-conserving way (Faucher-Giguère & Quataert 2012; Zubovas & King 2012). A more recent study by Fiore et al. (2017) has found tight correlations between the bolometric luminosity of AGNs and the mass outflow rates of MOs.

X-ray emission from AGNs probes the innermost energetic regions where matter is accreted onto a central SMBH. The emission from the accretion process for an SMBH of mass $\sim 10^7$–$10^8\,M_\odot$ peaks in the UV, and these photons get inverse Comptonized by a corona in AGNs to yield a power-law spectrum that extends into the hard X-rays. X-ray photons being less obscured by dust is a good probe of the SMBH

activity. In this work we carry out a systematic study of the 0.5–10 keV X-ray spectral properties of the sources exhibiting MOs (MOX sample hereafter). The main aim in this work is to characterize the X-ray properties of the MOX sample and investigate the effect of AGNs on the dynamical properties of MOs. Several sources in the MOX sample are luminous in infrared (see Section 2 for details). Previous studies on ultraluminous infrared galaxies (ULIRGs) revealed that these galaxies are underluminous in X-rays (Imanishi & Terashima 2004). A recent hard X-ray survey of six nearby ULIRGs using *NuSTAR* data (Teng et al. 2015) revealed similar findings. The unabsorbed 2–10 keV luminosity for these sources, when compared with the bolometric luminosity $L_{\rm bol}$ of the AGNs or the mid-IR [O IV] line luminosity, is found to be lower than that for Seyfert 1 galaxies. However, there are a few studies that have pointed out that the ULIRGs are not actually X-ray faint but extremely obscured. For example, a recent work on ULIRG UGC 5101 (Oda et al. 2017) with *NuSTAR* and *Swift* BAT telescopes has revealed that the intrinsic 2–10 keV luminosity of the source is $L_{2-10\ \rm keV} = 1.4 \times 10^{43}$ erg s^{-1}, which is ∼2.5 times larger than those obtained by previous estimates using X-ray spectra only up to 10 keV. The new value of $L_{2-10\ \rm keV}$ luminosity of UGC 5101 when compared with the luminosity of the 26 μm forbidden emission lines of [O IV] was found to be similar to Seyfert galaxies, indicating that the source is not X-ray weak. Ricci et al. (2017) in a sample study of LIRGs and ULIRGs found that these sources are heavily obscured by dust, and almost 65% of the sources in their sample were Compton thick. We should clearly note that estimating the intrinsic X-ray luminosity in these massive dusty galaxies is not straightforward owing to the largely unknown obscuration column density and the unknown geometry and composition of the obscurer.

This paper aims at addressing the following important questions:

1. Are the AGNs in the galaxies hosting MOs intrinsically X-ray weak?
2. Are AGNs the main driver of the large-scale MOs?

The paper is organized as follows: Section 2 describes the sample selection. It also includes the bolometric luminosity, the 12 μm luminosity, and MO properties of the MOX sample. Section 3 describes the X-ray observations for the MOX sample. Section 4 describes the methods employed for data analysis. Section 5 describes the correlation analysis. Section 6 discusses the results from the extensive X-ray analysis, followed by conclusions in Section 7.

2. Sample Description

We have selected a sample of 47 galaxies from published literature, which have exhibited MOs, as on 2016 October 20. Table 1 lists the sources, their redshift, and their spectral classification based on previous optical and X-ray studies. Table 2 lists the MO velocity and the mass outflow rates ($\dot{M}_{\rm out}$). These 47 sources define the MOX sample.

The MOs detected in the MOX sample are in the form of either OH absorption lines at 119, 79, and 65 μm or CO rotational-vibrational emission lines at 115 GHz, CO (1–0), using several state-of-the-art IR and radio telescopes such as VLT-SINFONI, *Herschel*-PACS, ALMA, Noema, and IRAM-PDBI. For the sources IRAS 17208−0014 and NGC 1433, the MO properties were derived using the transitions CO (2–1) and CO (3–2), respectively (see Table 2 and Section 2.1 for details).

From Table 2 we find that four sources have CO and OH detections of MO. In all cases the velocities measured by the two different outflows are consistent within errors, except for the source IRAS 17208–0014, where the CO measured a velocity of 600 km s^{-1} while OH measured a velocity of 100 km s^{-1}. We consider only the highest-velocity outflow in this case, which measures the maximum impact of the central engine on the host galaxy ISM. We should note that the OH absorption and the CO emission lines may be probing entirely different clumps of molecular gas at different locations in the host galaxy. However, we find that the distributions of MO velocity and mass outflow rates ($\dot{M}_{\rm out}$) estimated using OH absorption features or the CO emission lines are similar for the sources in the MOX sample. Hence, we treat the velocity and $\dot{M}_{\rm out}$ obtained using OH and CO methods on equal footings.

The MOX sample is not complete and can be biased toward infrared-bright objects, as most of these are ULIRGS or LIRGs. Figure 1 shows the distribution of the redshift of the galaxies in the sample, and we find that they are all in the local universe ($z < 0.2$).

2.1. Molecular Outflow Properties of the Sample

As noted earlier, Table 2 lists the MO properties of the sources along with the references from which they have been derived. We briefly describe in this section the methods used by different authors to estimate the MO properties and the threshold they have set for detecting an MO.

Sturm et al. (2011) detected the MO using the OH absorption lines at 79 and 119 μm observed using the *Herschel*-PACS telescope. The average error on the velocity estimated by the authors is 150 km s^{-1}. Veilleux et al. (2013) detected the MO using the OH absorption line 119 μm observed using the *Herschel*-PACS telescope. The average error on the velocity estimated by the authors is 50 km s^{-1}. The authors define a wind as an OH absorption profile whose median velocity (v_{50}) is more negative than −50 km s^{-1} with respect to the systemic velocity. In our work, we use the quantity v_{84} as the outflow velocity. v_{84} is the velocity above which 84% of the absorption of the OH profile takes place. Cicone et al. (2014) studied the MO in a sample of galaxies using CO (1–0) emission lines at 115.271 GHz, observed by the IRAM-PDBI telescope. The authors have relied on the simultaneous detection of OH absorption and CO emission lines for a given galaxy to detect MOs. In a few cases the authors could only put upper limits on velocity and hence could not effectively constrain the mass outflow rates. Stone et al. (2016) carried out a blind search for MOs in a sample of 52 local Seyfert galaxies using the OH 119 μm absorption line with *Herschel*-PACS data and detected MOs in three sources.

The MO velocities are in the range of ∼50–1000 km s^{-1} and the mass outflow rates are $\sim 10^{0.20}$–$10^{3.26}\ M_{\odot}$ yr^{-1}. The left panel of Figure 2 shows the distribution of MO velocity, and the right panel shows the distribution of mass outflow rates. From Table 2 we note that the mass outflow rates of the MOs are reported only for the first 27 sources, and for other sources they could not be calculated by the authors owing to the lack of distance estimates, because of insufficient spatial resolution.

2.2. The Bolometric Luminosity of the Sample

The total bolometric luminosity $L_{\rm bol}$ of the host galaxies, along with the references, is listed in Table 7. The values of

Table 1
List of Sources, Their General Properties, Previous X-Ray Studies, and the 12 μm Flux

Index	Source	Other Names	z	R.A.	Decl.	Classification[a]	Galaxy[b] Activity	References[c]	$F_{12\ \mu m}$[d] (mJy)
(1)	(2)	(3)	(4)	(5)	(6)	(7)	(8)	(9)	(10)
1	IRAS F08572+3915	⋯	0.0583	$09^h00^m25^s.3$	$+39^d03^m54^s.4$	ULIRG	CT	1, 2	325 ± 30
2	IRAS F10565+2448	⋯	0.0431	$10^h59^m18^s.1$	+24d32m34s	ULIRG	OA	2	200 ± 30
3	IRAS 23365+3604	⋯	0.0645	$23^h39^m01^s$	$+36^d21^m08^s$	ULIRG	OA/LINER	1	<0.09
4	Mrk 273	⋯	0.0377	$13^h44^m42^s.1$	$+55^d53^m13^s$	ULIRG	Sy2/OA	2	240 ± 17
5	Mrk 876	⋯	0.129	$16^h13^m57^s.2$	$+65^d43^m10^s$	⋯	Sy1		87 ± 12
6	I Zw 1	UGC 00545	0.0589	$00^h53^m34^s.9$	$+12^d41^m36^s$	Sy1	NLSy1		549 ± 11
7	MrK 231	⋯	0.0421	$12^h56^m14^s.2$	$+56^d52^m25^s$	ULIRG/RL	Sy1/SB	2	1830 ± 17
8	NGC 1266	⋯	0.0072	$03^h16^m00^s.7$	$-02^d25^m38^s$	Sy	AGN	3	250 ± 30
9	M82	⋯	0.0006	$09^h55^m52^s.7$	$+69^d40^m46^s$	⋯	SB	4	63000 ± 3150
10	NGC 1377	⋯	0.0059	$03^h36^m39^s.1$	$-20^d54^m08^s$	⋯	NC	5, 6	560 ± 20
11	NGC 6240	⋯	0.0244	$16^h52^m58^s.9$	$+02^d24^m03^s$	LIRG	CT/GM/SB	1	590 ± 25
12	NGC 3256	⋯	0.0093	$10^h27^m51^s.3$	$-43^d54^m13^s$	LIRG	SB	7	3570 ± 31
13	NGC 3628	⋯	0.0028	$11^h20^m17^s.0$	$+13^d35^m23^s$	RL	SB	8	3130 ± 48
14	NGC 253	⋯	0.0008	$00^h47^m33^s.1$	$-25^d17^m18^s$	⋯	Variable SB	9	41000 ± 35
15	NGC 6764	⋯	0.0081	$19^h08^m16^s.4$	$+50^d56^m00^s$	⋯	AGN+SB	10	310 ± 47
16	NGC 1068	⋯	0.0038	$02^h42^m40^s.7$	$-00^d00^m48^s$	LIRG	CT/Sy2	11	39800 ± 76
17	IC 5063	⋯	0.0113	$20^h52^m02^s.3$	$-57^d04^m08^s$	Sy1/RL	NLSy2	12	1110 ± 23
18	NGC 2146	⋯	0.0029	$06^h18^m37^s.7$	$+78^d21^m25^s$	LIRG	SB	13	7360 ± 800
19	IRAS 17208−0014	⋯	0.0428	$17^h23^m21^s.9$	$-00^d17^m01^s$	ULIRG/LINER	ULIRG	2	200 ± 25
20	NGC 1614	⋯	0.0159	$04^h33^m59^s.8$	$-08^d34^m44^s$	LIRG/SB	SB	14	1210 ± 111
21	IRAS 05083+7936	VII Zw 031	0.0536	$05^h16^m46^s.1$	$+79^d40^m13^s$	LIRG	OA	⋯	200 ± 26
22	IRAS 13451+1232	4C +12.50	0.1217	$13^h47^m33^s.3$	$+12^d17^m24^s$	ULIRG/RL	Sy2	2	<143
23	3C 293	UGC 08782	0.0450	$13^h52^m17^s.8$	$+31^d26^m46^s$	Sy/RL	NC	15	19 ± 2
24	NGC 1433		0.0035	$03^h42^m01^s.5$	$-47^d13^m19^s$	SB	NC	⋯	237 ± 17
25	IRAS 13120−5453	WKK 2031	0.0308	$13^h15^m06^s.3$	$-55^d09^m23^s$	ULIRG	NC	16	440 ± 27
26	IRASF 14378-3651	⋯	0.0676	$14^h40^m59^s$	$-37^d04^m32^s$	ULIRG	Sy2	1	<100
27	IRAS F11119+3257	B2 1111+32	0.1890	$11^h14^m38^s.9$	$+32^d41^m33^s$	ULIRG	NC	17	167 ± 27
28	IRAS F01572+0009	Mrk 1014	0.1631	$01^h59^m50^s.2$	$+00^d23^m41^s$	ULIRG/Sy1.5	NC	18	134 ± 40
29	IRAS F05024−1941	⋯	0.1920	$05^h04^m36^s.5$	$-19^d37^m03^s$	ULIRG	NC	2	<276
30	IRAS F05189−2524	⋯	0.0425	$05^h21^m45^s$	$-25^d21^m45^s$	ULIRG	Sy2	2	740 ± 16
31	IRAS 07251−0248	⋯	0.0875	$07^h27^m37^s.5$	$-02^d54^m55^s$	ULIRG	Faint src	1	<7
32	IRAS F07599+6508	⋯	0.1483	$08^h04^m33^s.1$	$+64^d59^m49^s$	ULIRG	NC	2	264 ± 23
33	IRAS 09022−3615	⋯	0.0596	$09^h04^m12^s.7$	$-36^d27^m01^s$	ULIRG	AGN	1	200 ± 32
34	IRAS F09320+6134	UGC 05101	0.0393	$09^h35^m51^s.6$	$+61^d21^m11^s$	ULIRG	OA	1	179 ± 16
35	IRAS F12072−0444	⋯	0.1284	$12^h09^m45^s.1$	$-05^d01^m14^s$	ULIRG/Sy2	NC	2	<119
36	IRAS F12112+0305	⋯	0.0733	$12^h13^m46^s.0$	$+02^d48^m38^s$	ULIRG	SB	1	<110
37	IRAS F14348−1447	⋯	0.0830	$14^h37^m38^s.4$	$-15^d00^m20^s$	ULIRG	CT/SB	1	108 ± 32
38	IRAS F14394+5332	⋯	0.1045	$14^h41^m04^s.4$	$+53^d20^m09^s$	ULIRG	NC	⋯	<72
39	IRAS F15327+2340	ARP 220	0.0181	$15^h34^m57^s.2$	$+23^d30^m11^s$	ULIRG/Sy	OA	2	496 ± 45
40	IRAS F15462−0450	⋯	0.0997	$15^h48^m56^s.8$	$-04^d59^m34^s$	ULIRG/NLSy1	NC	2	100 ± 30
41	IRAS F19297−0406	⋯	0.0857	$19^h32^m21^s.2$	$-03^d59^m56^s$	ULIRG	NC	1	<100
42	IRAS 19542+1110	⋯	0.0649	$19^h56^m35^s.4$	$+11^d19^m03^s$	ULIRG	OA	1	80
43	IRAS F20551−4250	ESO 286IG019	0.0429	$20^h58^m26^s.8$	$-42^d39^m00^s$	ULIRG	CT	1	280 ± 21
44	IRAS F23233+2817	⋯	0.1140	$23^h25^m49^s.4$	$+28^d34^m21^s$	ULIRG/Sy2	NC	⋯	<129
45	NGC 5506	⋯	0.0062	$14^h13^m14^s.9$	$-03^d12^m27^s$	Sy	NC	19	1480 ± 90

Table 1
(Continued)

Index	Source	Other Names	z	R.A.	Decl.	Classification[a]	Galaxy Activity[b]	References[c]	$F_{12\ \mu m}$[d] (mJy)
(1)	(2)	(3)	(4)	(5)	(6)	(7)	(8)	(9)	(10)
46	NGC 7479	⋯	0.0079	$23^h04^m56\overset{s}{.}6$	$+12^d19^m22^s$	SB/Sy1.9	NC	20	1390 ± 30
47	NGC 7172		0.0087	$22^h02^m01\overset{s}{.}9$	$-31^d52^m11^s$	Sy2	NC	21	720 ± 60

Notes.
[a] The classification as obtained from NED.
[b] The galaxy activity as identified by previous X-ray and optical studies: CT = Compton thick; CL = changing look; OA = obscured AGN; LINER = low-ionization nuclear emission line region; Sy2 = Seyfert 2; NLSy1 = narrow-line Seyfert 1; SB = starburst; GM = galaxy mergers; NC = not classified.
[c] The references to the previous X-ray studies: (1) Iwasawa et al. 2011; (2) Teng & Veilleux 2010; (3) Alatalo et al. 2015; (4) Liu et al. 2014; (5) Costagliola et al. 2016; (6) Aalto et al. 2016; (7) Lehmer et al. 2015; (8) Tsai et al. 2012; (9) Krips et al. 2016; (10) Croston et al. 2008; (11) Marinucci et al. 2016; (12) Cicone et al. 2014; (13) Inui et al. 2005; (14) Herrero-Illana et al. 2014; (15) Lanz et al. 2015; (16) Teng et al. 2015; (17) Tombesi et al. 2015; (18) Ricci et al. 2014; (19) Guainazzi et al. 2010; (20) Akylas & Georgantopoulos 2009; (21) Guainazzi et al. 1998.
[d] The 12 μm monochromatic flux of the galaxies obtained from NASA Extragalactic Database.

L_{bol} include the AGN and the stellar contribution from the host galaxies calculated using the integrated infrared luminosity (8–1000 μm) and following the scaling relation $L_{bol} = 1.12L_{IR}$ (Veilleux et al. 2013; Cicone et al. 2014). We also list the AGN fraction, α_{AGN}, for each source calculated using the IR flux ratios, $f_{15\ \mu m}/f_{30\ \mu m}$ (Veilleux et al. 2013). The bolometric luminosity of the central AGN is calculated as $L_{AGN} = \alpha_{AGN} \times L_{bol}$. The starburst (SB) luminosities from the galaxies are calculated using $L_{Starburst} = (1 - \alpha_{AGN}) \times L_{bol}$.

2.3. The 12 μm Luminosity of the Sample

Gandhi et al. (2009) have found a strong correlation between the 12 μm luminosity from the inner core of active galaxies and the 2–10 keV AGN X-ray luminosity ($L_{2-10\ keV}$), indicating the effects of dust being heated by the central AGN, which then re-emits in the IR. Thus, the 12 μm luminosity can be used as a probe for the $L_{2-10\ keV}$ AGN emission for the MOX sources. However, obtaining the 12 μm flux of the spatially resolved inner core of the MOX galaxies is beyond the scope of the paper. Hence, we use the 12 μm values quoted in the NASA Extragalactic Database (NED) obtained using the *Infrared Astronomical Satellite* (*IRAS*) observatory. Since this is the emission from the whole galaxy, we must remember that the 12 μm luminosity can have contributions from both the AGN and stellar emission. In order to obtain an estimate of the AGN contribution to the 12 μm emission, we multiply the values obtained from NED by α_{AGN} as described in the previous section and then use this quantity in the correlation in Asmus et al. (2015), given by $\log(L_{2-10\ keV}/10^{43}\ erg\ s^{-1}) = -0.32 + 0.95 \times \log(L_{12\ \mu m} \times \alpha_{AGN}/10^{43}\ erg\ s^{-1})$. However, we note that the $L_{2-10\ keV}$ obtained using this method is possibly an upper limit to the intrinsic AGN emission, as there can be other mechanisms in the host galaxy contributing to the 12 μm flux (see Section 6.1 for a discussion). Table 6 lists the values of the $L_{2-10\ keV}$ obtained using this method. See Figure 3 for a comparison of the $L_{2-10\ keV}$ estimated using the 12 μm luminosity and that directly measured via X-ray spectroscopy.

3. X-Ray Observations and Data Reduction

We have used broadband X-ray spectra from *XMM-Newton* EPIC-pn and *Chandra* ACIS CCD telescopes, which give an energy coverage of 0.3–10 keV and 0.6–10 keV, respectively. For sources where there are multiple observations, we have considered only the longest observation to maximize the signal-to-noise ratio (S/N) irrespective of the flux or spectral state of the source. Table 3 shows the list of X-ray observations used for the MOX sample. All the data used in this work are publicly available in the *XMM-Newton* and *Chandra* archives.

The *XMM-Newton* EPIC-pn data were downloaded and reduced using the standard Scientific-Analysis-System (SAS) software, version 15. Calibrated and concatenated event lists for the EPIC-pn camera were generated using the SAS task *epchain*. Good time intervals for the accumulation of scientific products were defined as those with particle background count rate $R \leqslant 1$ counts s^{-1} above 10 keV. The source region was selected using a circle of radius 40″ with the center of the circle fixed to the R.A. and decl. of the source obtained from NED. The background regions were selected from regions away from the source but from the same CCD. There was no photon pileup for any of the sources, which we checked using the command *epatplot*.

The *Chandra* data were reprocessed using the software CIAO, version 4.7.1. The source regions were extracted from circles of radius 2.5″ with the center of the circle fixed to the R.A. and decl. of the source. The background regions were selected from regions away from the source but from the same CCD. The command *specextract* was used to extract the source+background spectra, the background spectra, the effective area (ARF), and the redistribution matrix. In the MOX sample there are 16 sources for which we have used *Chandra* observations. Appendix A lists the X-ray spectra, the best-fit models, and the residuals of the MOX sources. In Appendix B we describe the previous studies of the sources in the MOX sample, as well as listing the details of the X-ray spectral modeling carried out in this work.

4. X-Ray Spectral Analysis

For the 39 out of 47 sources where the total photon count is >200 (see Table 3) we have used a combination of mostly phenomenological models, step by step, to fit the spectra. The S/N of several sources in the MOX sample is not sufficiently high to obtain statistically meaningful results with complex models. The simple baseline model consists of a power law absorbed by Galactic extinction (Kalberla et al. 2005). A further intrinsic absorber (*ztbabs*) was added if the source exhibited obscuration. The model APEC (Smith et al. 2001) was used to describe emission in the soft X-rays. In a few cases two APEC models were necessary to describe the soft X-ray

Table 2
List of Sources and Their Properties

Index	Source	Method Used	Reference	Outflow Velocity[a] km s^{-1}	$\dot{M}_{\rm out}$ $\log(M_\odot\ {\rm yr}^{-1})$	SFR $(M_\odot\ {\rm yr}^{-1})$	
1	IRAS F08572+3915[b]	CO (1–0)	1	800 ± 160	3.082	20	
	〃	OH	2	700 ± 140	2.98	⋯	
2	IRAS F10565+2448	CO (1–0)	1	450 ± 90	2.477	95	
3	IRAS 23365+3604	CO (1–0)	1	450 ± 90	2.230	137	
4	Mrk 273	CO (1–0)	1	620 ± 124	2.778	139	
5	Mrk 876	CO (1–0)	1	700 ± 140	$\leqslant$3.262	6.5	
6	I Zw 1	CO (1–0)	1	500 ± 100	$\leqslant$2.146	36	
7	MrK 231[1]	CO (1–0)	1	700 ± 140	3.02	234	
	〃	OH	2	600 ± 120	3.07	⋯	
8	NGC 1266	CO (1–0)	1, 3	177 ± 100	1.518–2.255	1.6	
9	M82	CO (1–0)	1, 4	100 ± 100	1.079–1.255	10	
10	NGC 1377	CO (1–0)	1 5	110 ± 100	1.146–1.881	0.9	
11	NGC 6240	CO (1–0)	1, 6	400 ± 100	2.903	16	
12	NGC 3256	CO (1–0)	1, 7	250 ± 100	1.041–1.204	36	
13	NGC 3628	CO (1–0)	1, 8	50 ± 100	0.653–0.826	1.8	
14	NGC 253[1]	CO (1–0)	1, 9	50 ± 100	0.623–0.799	3	
	〃	OH	2	75 ± 100	0.20	⋯	⋯
15	NGC 6764	CO (1–0)	1, 10	170 ± 100	0.491–0.672	2.6	
16	NGC 1068	CO (1–0)	1, 11	150 ± 100	1.924	18	
17	IC 5063	CO (1–0)	1, 12	300 ± 100	1.361–2.103	0.6	
18	NGC 2146	CO (1–0)	1, 13	150 ± 100	1.146–1.342	12	
19	IRAS 17208−0014[1]	CO (2–1)	14	600 ± 100	2.518	⋯	
	〃	OH	2	100 ± 100	1.954	⋯	
20	NGC 1614	CO (1–0)	14	360 ± 100	1.602	⋯	
21	IRAS 05083+7936	CO (1–0)	15	750 ± 100	⋯	⋯	
22	IRAS 13451+1232	CO (1–0)	16	750 ± 50	2.361–2.903	⋯	
23	3C 293	CO (1–0)	17	350 ± 100	1.397–1.477	⋯	
24	NGC 1433	CO (3–2)	18	200 ± 100	0.845	⋯	
25	IRAS 13120−5453	OH	2	520 ± 150	2.113	⋯	
26	IRAS 14378−3651	OH	2	800 ± 150	2.869	⋯	
27	IRAS F11119+3257	OH	19	1000 ± 200	$2.903^{+0.400}_{-0.501}$	⋯	
28	IRAS F01572+0009	OH	20	892 ± 50	⋯	⋯	
29	IRAS F05024−1941	OH	20	508 ± 50	⋯	⋯	
30	IRAS F05189−2524	OH	20	574 ± 50	⋯	⋯	
31	IRAS 07251−0248	OH	20	255 ± 50	⋯	⋯	
32	IRAS F07599+6508	OH	20	1000 ± 50	⋯	⋯	
33	IRAS 09022−3615	OH	20	297 ± 50	⋯	⋯	
34	IRAS F09320+6134	OH	20	225 ± 50	⋯	⋯	
35	IRAS F12072−0444	OH	20	321 ± 50	⋯	⋯	
36	IRAS F12112+0305	OH	20	237 ± 50	⋯	⋯	
37	IRAS F14348−1447	OH	20	508 ± 50	⋯	⋯	
38	IRAS F14394+5332	OH	20	495 ± 50	⋯	⋯	
39	IRAS F15327+2340	OH	20	153 ± 50	⋯	⋯	
40	IRAS F15462−0450	OH	20	459 ± 50	⋯	⋯	
41	IRAS F19297−0406	OH	20	532 ± 50	⋯	⋯	
42	IRAS 19542+1110	OH	20	489 ± 50	⋯	⋯	
43	IRAS F20551−4250	OH	20	748 ± 50	⋯	⋯	
44	IRAS F23233+2817	OH	20	423 ± 50	⋯	⋯	
45	NGC 5506	OH	21	357 ± 50	⋯	⋯	
46	NGC 7479	OH	21	658 ± 50	⋯	⋯	
47	NGC 7172	OH	21	207 ± 50	⋯	⋯	

Notes.
[a] Different authors have used +ve and −ve notations to denote outflow velocities (blueshifted) with respect to the systemic velocity. To avoid confusion and maintain uniformity, we have considered the modulus of the velocities.
[b] Sources that have been observed both by CO and OH molecules.

References. (1) Cicone et al. 2014; (2) Sturm et al. 2011; (3) Alatalo et al. 2011; (4) Walter et al. 2002; (5) Aalto et al. 2012; (6) Feruglio et al. 2013; (7) Sakamoto et al. 2006; (8) Tsai et al. 2012; (9) Mauersberger et al. 1996; (10) Sanders & Mirabel 1985; (11) Maiolino et al. 1997; (12) Wiklind et al. 1995; (13) Tsai et al. 2006; (14) García-Burillo et al. 2015; (15) Leroy et al. 2015; (16) Dasyra et al. 2014; (17) Labiano et al. 2014; (18) Combes et al. 2013; (19) Tombesi et al. 2015; (20) Veilleux et al. 2013; (21) Stone et al. 2016.

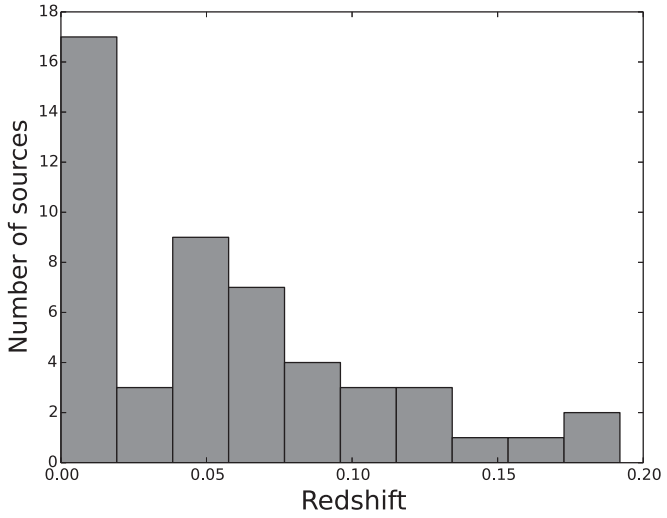

Figure 1. Redshift distribution of the MOX sources.

emission. A simple blackbody model was used in two sources (I ZW 1 and NGC 7172) where the APEC did not give a good fit. For sources with higher S/N, Gaussian profiles were used to describe the emission lines in both soft and hard X-ray, especially the Fe K features in the 6–8 keV band. These narrow soft emission lines arise mostly as a result of photoionization of the plasma by the central source, or reprocessing of the nuclear high-energy primary continuum by optically thick matter. The *diskline* profile was used to model the broad Fe Kα profile, wherever present.

The *XMM-Newton* EPIC-pn data were grouped using the *specgroup* command in SAS, by which we ensured that each data bin has at least 20 counts and there are at most five data bins per resolution element. The *Chandra* observations were grouped by a minimum S/N of 2. We used χ^2 statistics to fit the data. All errors quoted on the fitted parameters reflect the 90% confidence interval for one interesting parameter corresponding to $\Delta\chi^2 = 2.7$ (Lampton et al. 1976). The Interactive Spectral Interpretation System software (Houck & Denicola 2000) was used in fitting the spectra.

Table 4 lists the best-fit parameters along with the 0.6–2 keV and 2–10 keV absorption-corrected flux and luminosity. The 0.6–2 keV luminosity quoted in the table is from the model APEC only and not the integrated continuum flux. We assume hereafter that the model APEC describes the thermal emission in the soft X-rays mostly arising from supernova remnants and SBs (see, e.g., Ducci et al. 2013; Mitsuishi et al. 2013). The best-fit temperatures of APEC lie in the range $\sim kT = 0.08$–1 keV. In most cases the AGN continuum is absorbed below 2 keV, and from Table 4 we find that almost all the sources with sufficient S/N have a neutral intrinsic column density of $\sim 10^{21} - 10^{22}$ cm^{-2}. However, as a caveat we should note that in some cases the soft X-rays may also contain contributions from the reprocessed emission from the central AGN, such as ionized disk reflection, and can mimic thermal emission (see Appendix B, Figure 10; the show the data and the best-fit model is shown in the top panels, and the residuals are shown in the bottom panels). Note that for the two sources M82 and NGC 1068 the soft X-ray spectra were extremely complex and could not be fit using the simple baseline model.

For the sources where the S/N does not permit us to constrain simultaneously the power-law slope and the neutral absorption column, we fix the slope to a value $\Gamma = 1.8$, typical of Seyfert galaxies, and calculate the corresponding fluxes and absorption column. See Table 4 for details. For the seven Compton-thick sources (NGC 6240, NGC 1068, NGC 1377, IRAS F08572+3915, IRAS F20551−4250, IRAS F14348 −1447, IRAS 13120−5453) in our sample identified from previous studies, we have multiplied the observed $L_{2-10\,\mathrm{keV}}$ by a factor of 100 to obtain the intrinsic $L_{2-10\,\mathrm{keV}}$ while carrying out the correlation analysis (see, e.g., Lamastra et al. 2009; Puccetti et al. 2016). See Table 5 for the final $L_{2-10\,\mathrm{keV}}$ values of these sources and Section 4.1 for details.

For eight sources in the MOX sample, having total counts <200, we have used the 2–10 keV luminosity from previous studies that have employed the hardness ratio method (e.g., Teng & Veilleux 2010). The hardness ratio is defined as HR = (H–S)/(H+S), where H and S are the number of counts in the hard (2–8 keV) and soft (0.5–2.0 keV) bands, respectively. The hardness ratios calculated from the data were then compared with hardness ratios generated with an absorbed power-law model to estimate the model parameters (Teng et al. 2005).

4.1. Assembling the Best Values of $L_{2-10\,keV}$ Estimated Using X-Ray Spectroscopy

As inferred from Section 4, most of the sources in the MOX sample are probably obscured by the intervening host galaxy dust and gas, and therefore the 2–10 keV luminosity estimated from the X-ray spectral analysis of *XMM-Newton* and *Chandra* may not give us the real picture. A better glimpse of the unobscured $L_{2-10\,\mathrm{keV}}$ luminosities can be obtained by analyzing spectra at energies >10 keV, where the hard X-ray photons have lesser probability to get absorbed. *NuSTAR* operates in the energy range ∼3–40 keV and gives us the unique opportunity of such an intrinsic view of the $L_{2-10\,\mathrm{keV}}$ luminosity. In this section we discuss how we selected the best estimate of $L_{2-10\,\mathrm{keV}}$ available to us by different X-ray spectral analysis methods.

We assigned the highest preference to the unabsorbed $L_{2-10\,\mathrm{keV}}$ values estimated using *NuSTAR*, whenever available. Only 23 sources in the MOX sample have been observed by *NuSTAR* either as targets or serendipitously. We carried out a literature search on the analysis of *NuSTAR* data of these sources and found that out of these 23, only 10 sources have enough S/N to carry out a spectral study in the broadband 3–40 keV. For example, the *NuSTAR* observations of the sources IRAS F08572+3915 and IRAS F10565+2448 found no detectable X-ray signatures in the 3–40 keV energy band (Teng et al. 2015). The intrinsic $L_{2-10\,\mathrm{keV}}$ values for the 10 sources obtained with *NuSTAR* have been quoted in Table 5, along with the references from where they have been derived. For a list of the MOX sources not observed by *NuSTAR* see Appendix C. For the rest of the MOX sources we use the $L_{2-10\,\mathrm{keV}}$ estimated from the *XMM-Newton* and *Chandra* spectroscopy and the HR method enumerated in Section 4. For sources that have been previously identified as C-thick and have not been studied by *NuSTAR*, we have multiplied the $L_{2-10\,\mathrm{keV}}$ values obtained using the *XMM-Newton* and *Chandra* spectroscopy by a factor of 100 (see, e.g., Lamastra et al. 2009; Puccetti et al. 2016), to obtain an estimate of the intrinsic unabsorbed 2–10 keV luminosity.

Column (3) of Table 5 lists the $L_{2-10\,\mathrm{keV}}$ values obtained using *XMM-Newton* and *Chandra* spectroscopy, while Column (4) lists

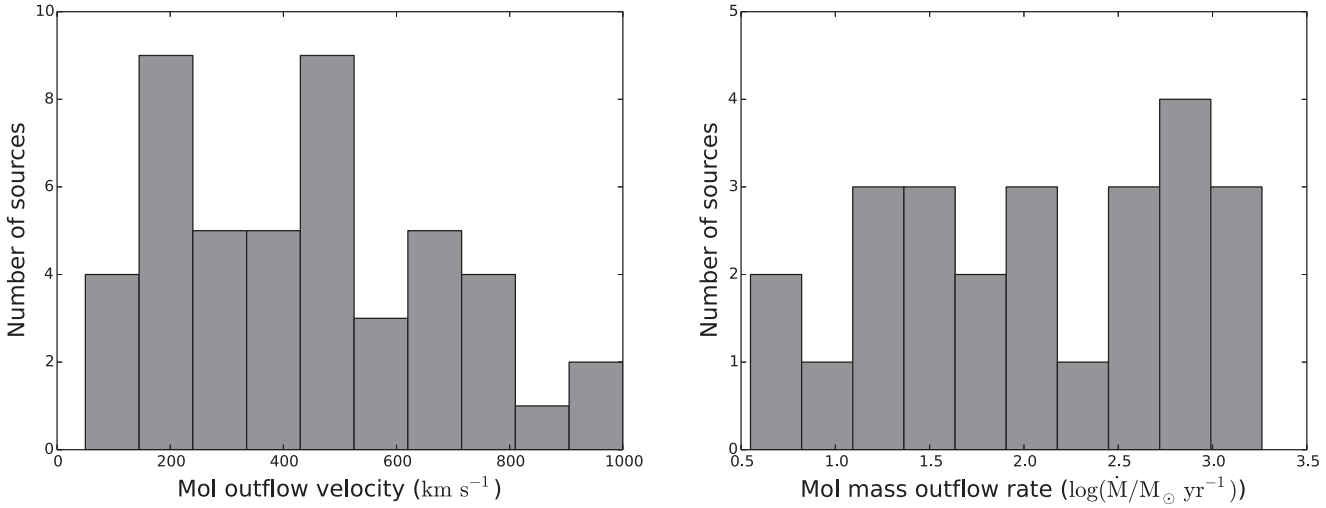

Figure 2. Left: distribution of MO velocity. Right: distribution of the MO mass outflow rate.

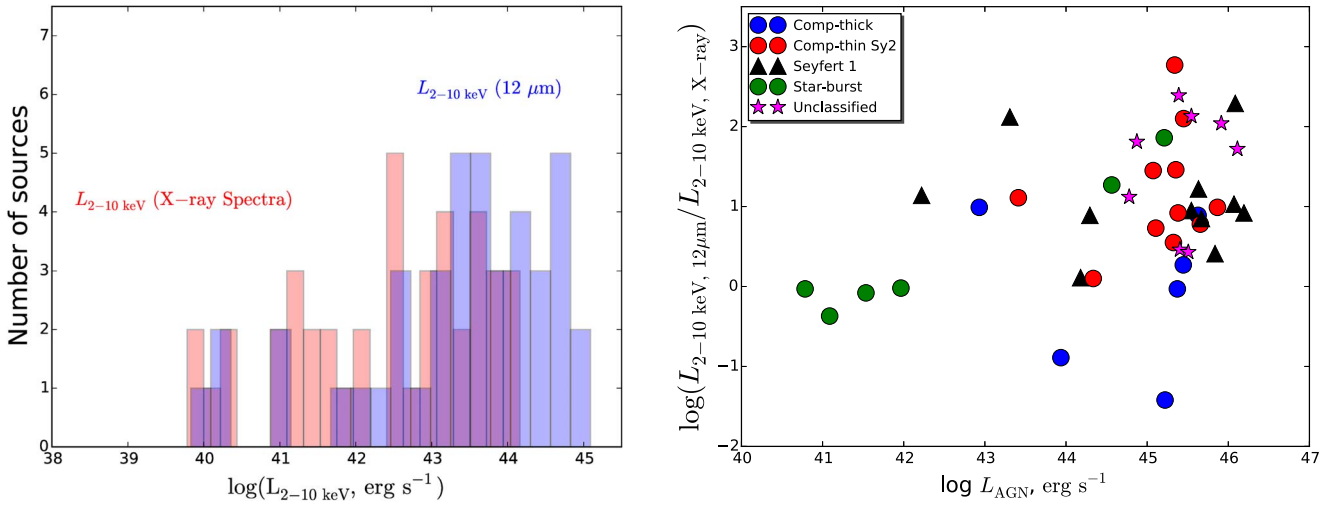

Figure 3. Left: 2–10 keV luminosity, $L_{2\text{–}10\ \mathrm{keV}}$, distribution of the MOX sources calculated by the two methods, X-ray spectroscopy (in pink color) and 12 μm luminosity (in blue color), as described in Sections 2.3 and 4.1. Right: ratio between the $L_{2\text{–}10\ \mathrm{keV}}$ calculated using the two methods plotted against the bolometric luminosity of the AGN L_{AGN} of the MOX sources. The classification of source types is obtained from NED and from previous optical and X-ray studies. See Section 2 and Table 1 for details. The blue circles, red circles, black triangles, green circles, and magenta stars denote Compton-thick, Compton-thin, Seyfert 1, SB, and unclassified sources, respectively. We use this classification consistently throughout the paper.

the $L_{2\text{–}10\ \mathrm{keV}}$ values obtained using *NuSTAR*. The last column of Table 5 lists the best values of $L_{2\text{–}10\ \mathrm{keV}}$ we use in the rest of this work for analysis, which we refer to as $L_{2-10\ \mathrm{keV,\ X\text{-}ray\ spectra}}$. In Table 6 we compare the finally selected $L_{2\text{–}10\ \mathrm{keV}}$ values with those estimated using the 12 μm flux ($L_{2-10\ \mathrm{keV,\ 12\,\mu m}}$). The left panel of Figure 3 shows the distribution of the best $L_{2\text{–}10\ \mathrm{keV}}$ estimated above and the $L_{2\text{–}10\ \mathrm{keV}}$ estimated using 12 μm flux. The right panel of Figure 3 shows the ratio $L_{2-10\ \mathrm{keV,\ 12\,\mu m}}/L_{2-10\ \mathrm{keV,\ X\text{-}ray\ spectra}}$ plotted against the bolometric luminosity of the AGN (L_{AGN}).

The bolometric corrections ($L_{2\text{–}10\ \mathrm{keV}}/L_{\mathrm{bol}}$) corresponding to the two sets of $L_{2\text{–}10\ \mathrm{keV}}$ values are listed in Table 7. The left and right panels of Figure 4 show the bolometric corrections of the MOX sources with $L_{2-10\ \mathrm{keV,\ X\text{-}ray\ spectra}}$ and $L_{2-10\ \mathrm{keV,\ 12\,\mu m}}$ values, respectively, plotted against the bolometric luminosity of the AGN. In the left panel of Figure 4 we have plotted with yellow triangles the bolometric corrections of the sources for which the $L_{2\text{–}10\ \mathrm{keV}}$ were obtained using *NuSTAR* broadband spectroscopy. *NuSTAR* provides an accurate estimate of the intrinsic $L_{2\text{–}10\ \mathrm{keV}}$ luminosity, and hence the bolometric corrections obtained using those estimates are more reliable.

5. Correlations

To test the dependence of MO kinematics on AGN activity, we have correlated the X-ray luminosity in the two energy bands, $L_{0.6\text{–}2\mathrm{keV}}$ (APEC) and $L_{2\text{–}10\ \mathrm{keV}}$, as well as the AGN bolometric luminosity L_{AGN} with the MO velocity and mass outflow rates ($\dot{M}_{\mathrm{out}}$). We have also correlated the SB luminosity, $L_{\mathrm{Starburst}}$, with MO velocity and mass outflow rates. Table 8 lists the nonparametric Spearman rank coefficient, the null hypothesis probability, and the linear regression slope and intercept for these correlations. The number of data points involved in each correlation is also quoted in Table 8. The difference in the number of data points arises as a result of the fact that some of the sources in the MOX sample do not have mass outflow rate estimates, and also for a few sources we do

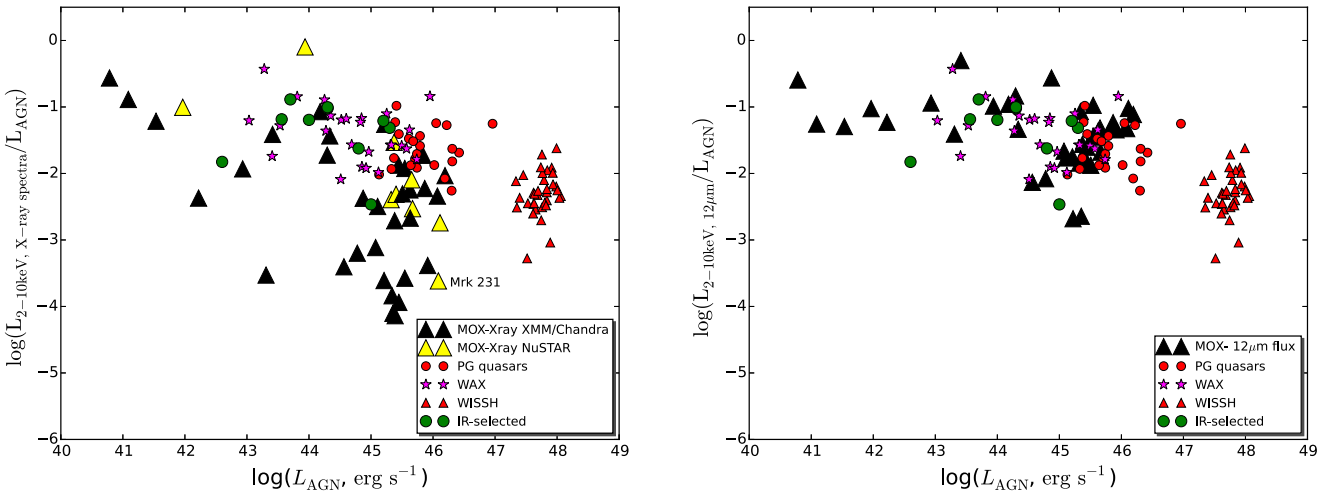

Figure 4. Left: X-ray bolometric correction $\log(L_{2-10\ keV}/L_{AGN})$ vs. L_{AGN} of the MOX sources along with the WAX (Laha et al. 2014), PG quasars (Laor et al. 1994), WISSH quasars (Martocchia et al. 2017), and the 12 μm selected AGNs (Brightman & Nandra 2011), as described in Section 6.1. Here the $L_{2-10\ keV}$ values of the MOX sources have been estimated using the method described in Section 4.1 and listed in Table 5. As *NuSTAR* gives us the best estimate of the unabsorbed $L_{2-10\ keV}$, we have plotted those sources in yellow triangles to separate them from those estimated using *XMM-Newton* and *Chandra* spectroscopy. Right: same as the left panel, but here the $L_{2-10\ keV}$ of the MOX sources are estimated using 12 μm luminosity.

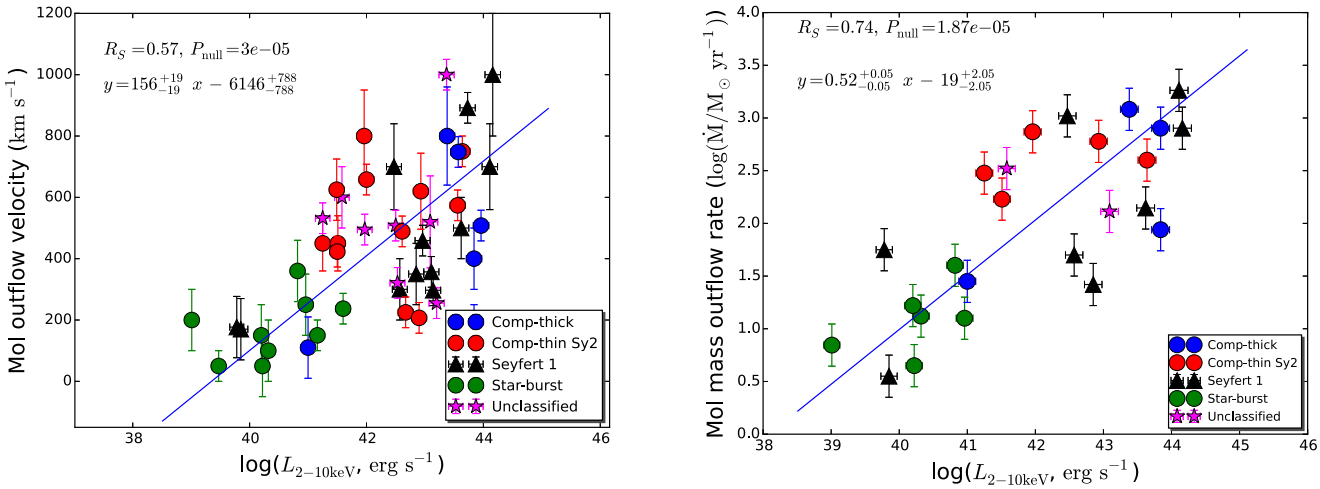

Figure 5. Left: correlation between the MO velocity and the 2–10 keV unabsorbed luminosity of the MOX sources obtained using X-ray spectroscopy as described in Section 4.1. Right: correlation between the molecular mass outflow rate and the 2–10 keV unabsorbed luminosity of the sources. We have assumed an error of 0.2 dex on the molecular mass outflow rates uniformly.

not have an estimate of the $L_{0.6-2keV}$ (APEC) and L_{AGN}. Figures 5–9 show the correlation between the $L_{0.6-2keV}$ (APEC), $L_{2-10\ keV}$, L_{AGN}, and $L_{Starburst}$ luminosities with the MO dynamical parameters (v and $\dot{M}_{out}$). The SB galaxies are plotted in green circles, and they occupy the phase space of lowest X-ray and AGN luminosity and lowest MO velocity, as well as the mass outflow rates. The black triangles, red circles, and blue circles denote the Seyfert 1 galaxies, Compton-thin Seyfert 2 galaxies, and Compton-thick galaxies, respectively. The magenta stars denote the unclassified sources.

From Figures 5 and 6 we find that the 2–10 keV luminosities of the MOX sources, $L_{2-10\ keV,\ X\text{-}ray\ spectra}$ and $L_{2-10\ keV,\ 12\ \mu m}$, respectively, show strong correlation with MO velocity and $\dot{M}_{out}$, with a confidence >99.99%. In both figures we find that the mass outflow rate $\dot{M}_{out}$ correlates better than that of the MO velocity. Similarly, Figure 7 shows that both the MO velocity and $\dot{M}_{out}$ strongly correlate with the AGN bolometric luminosity, with a confidence >99.99%. From Figures 8 and 9 we find that $L_{0.6-2keV}$ and $L_{Starburst}$ correlate with the MO velocity and $\dot{M}_{out}$ with a confidence >99%, but the correlations are not as strong as those with the AGN X-ray and bolometric luminosity. We discuss the implications of these results in Section 6.

We have used the freely available Python code by Nemmen et al. (2012) using the BCES technique (Akritas & Bershady 1996) to carry out the linear regression analysis between the quantities mentioned above. In this method the errors in both variables defining a data point are taken into account, as is any intrinsic scatter that may be present in the data, in addition to the scatter produced by the random variables. The strength of the correlation analysis was tested using the nonparametric Spearman rank correlation method.

6. Results and Discussion

We have carried out a uniform X-ray spectral analysis of a sample of 47 sources exhibiting MOs and obtained the best estimates of $L_{2-10\ keV}$ values using X-ray spectroscopy. We

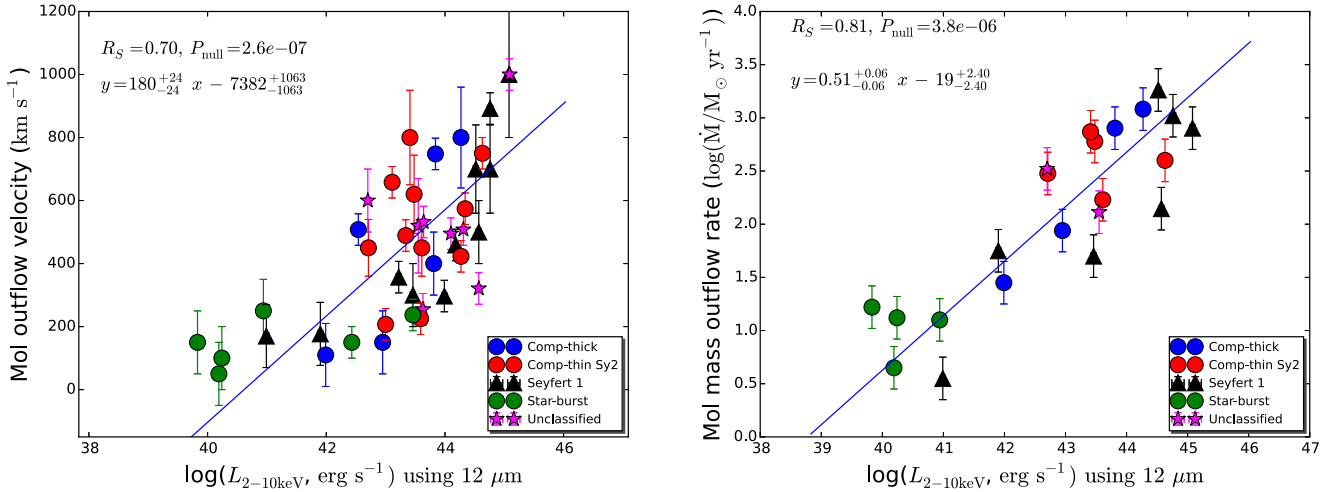

Figure 6. Left: same as Figure 5, except that the 2–10 keV luminosity has been obtained using the 12 μm flux, as described in Section 2.3. Right: same as Figure 5, except that the 2–10 keV luminosity has been obtained using the 12 μm flux.

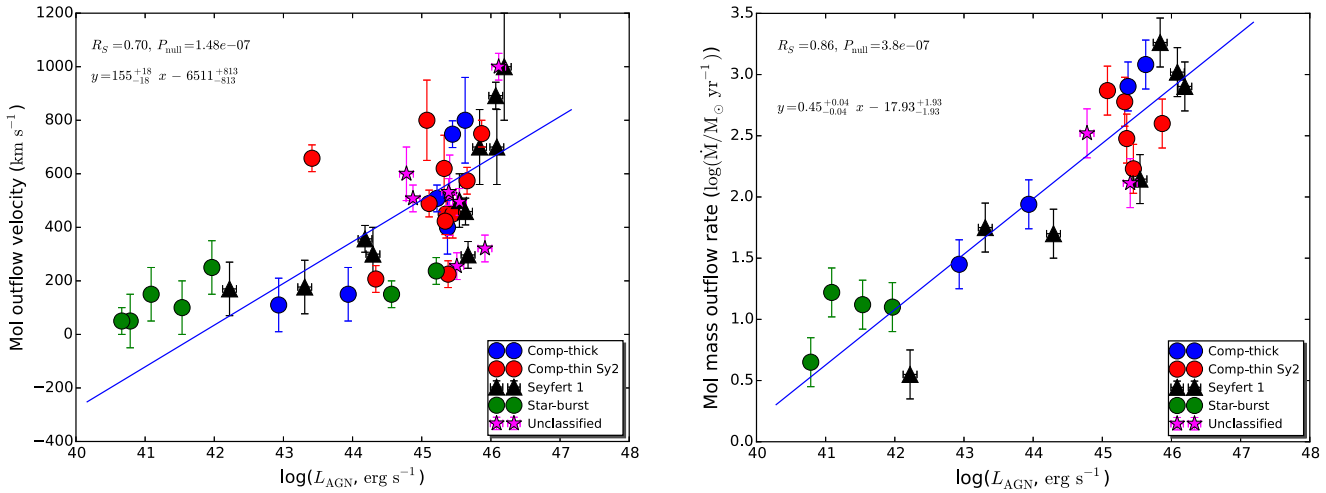

Figure 7. Left: correlation between MO velocity and AGN bolometric luminosity, $L_{\rm AGN}$. Right: correlation between mass outflow rate and AGN bolometric luminosity. Symbol description as in Figure 3.

have also estimated the $L_{2-10\,\rm keV}$ luminosity using 12 μm flux. As a caveat, we note that estimating the intrinsic X-ray luminosity in these massive dusty galaxies is not straightforward owing to large uncertainties in the obscuration along the line of sight, and most estimates are based on several assumptions. In this section we discuss the main results.

6.1. Are the AGNs in the MOX Sources X-Ray Weak?

The MOX sources are bright in IR, and hence it is possible that large columns of neutral gas and dust obscure our line of sight and we do not observe the intrinsic $L_{2-10\,\rm keV}$ for most of the galaxies. In this section we therefore investigate whether the MOX sources are extremely Compton thick or the AGNs at the center of the galaxies are indeed X-ray weak.

The NED classification of the MOX sources as listed in Table 1 shows that 33 out of 47 sources are ULIRGs or LIRGs, implying that they have large columns of gas and dust emitting in the infrared. A systematic study of the ULIRGs in the X-rays using the broadband *Chandra* and *XMM-Newton* data was carried out by Teng & Veilleux (2010), and the authors noted that possibly in the ULIRGs we are capturing the nascent stages of AGN activity (Sanders et al. 1988), in which case the central AGN emission could be weak and SB emission dominates the total power. In a more recent study by Teng et al. (2015) using *NuSTAR* observations of six ULIRGs, the authors conclude that these sources are indeed X-ray weak and not obscured. The typical example is that of Mrk 231, which is a merger remnant containing both intense SB and a luminous AGN at its center. Mrk 231, which was earlier thought to be a Compton-thick AGN, was found by the authors to be intrinsically X-ray weak using the 4–80 keV *NuSTAR* spectra (Teng et al. 2014). The X-ray bolometric corrections ($L_{2-10\,\rm keV}/L_{\rm AGN}$) estimated by the authors for the six sources in their sample were found in the range from 8×10^{-4} to 10^{-2}, indicating that the AGNs at the center of these sources are X-ray weak. Particularly for the two sources Mrk 231 and IRAS 08572+3915, they are remarkably low, at $\sim 5 \times 10^{-4}$ and $<10^{-4}$, respectively. Normally for Seyfert galaxies these values lie in the range 0.02–0.15 (see, e.g., Elvis et al. 1994; Vasudevan et al. 2009, 2010, and references therein). The authors rule out obscuration as the cause for the X-ray

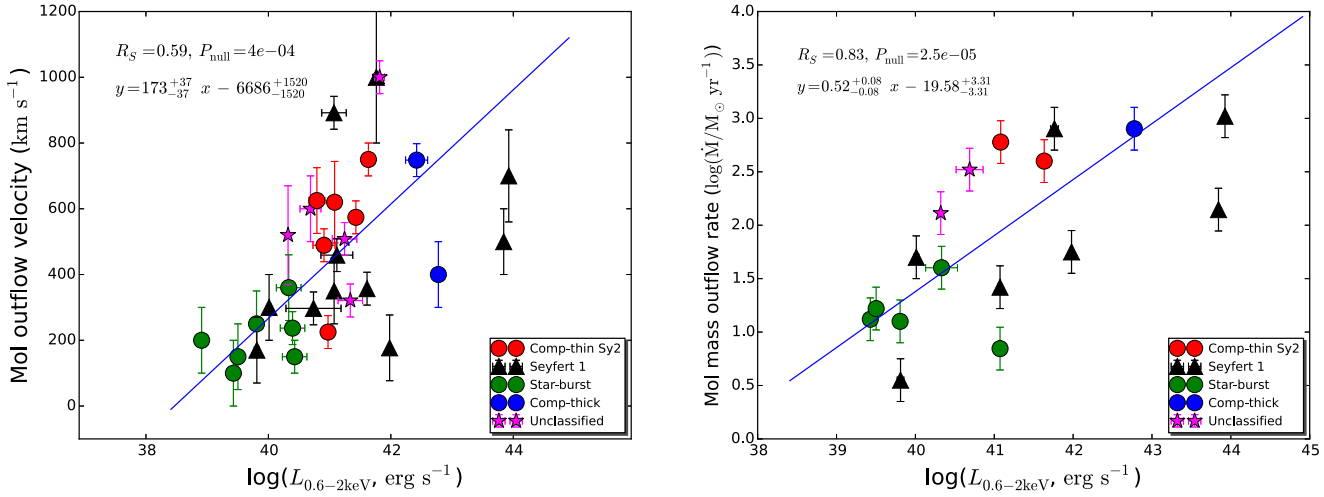

Figure 8. Left: dependence of MO velocity on the 0.6–2 keV APEC luminosity. Right: dependence of MO mass outflow rate on the 0.6–2 keV APEC luminosity. Symbol description as in Figure 3.

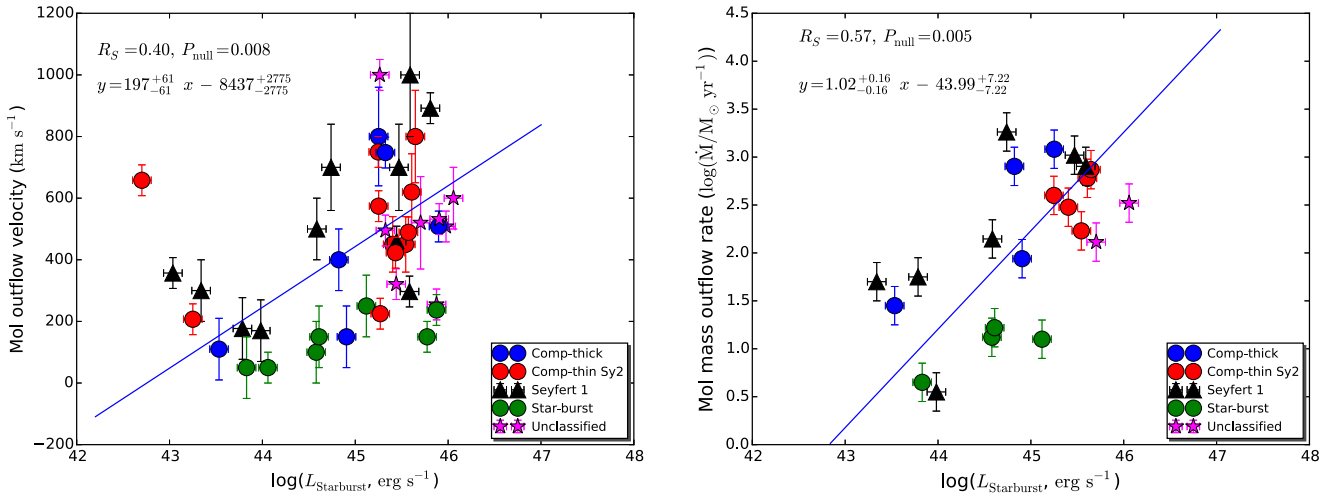

Figure 9. Left: dependence of MO velocity on the SB luminosity, $L_{\rm Starburst}$, as calculated in Section 2.2. Right: dependence of MO mass outflow rate on the SB luminosity. Symbol description as in Figure 3.

weakness. They conclude that possibly the AGN is accreting at super-Eddington rates, in which case the UV bump dominates, or else the presence of large-scale outflows may have quenched the X-ray emission in the AGN.

From the left panel of Figure 4 and Table 7, we find that the distribution of the bolometric correction ($L_{2-10\ \rm keV}/L_{\rm AGN}$) of the MOX sample ranges from $10^{-4.5}$ to $10^{-0.5}$, with 70% of the sources having X-ray bolometric correction below 10^{-2}. To compare the bolometric correction of the MOX sources with Seyfert and quasars, we selected four AGN samples at different redshift ranges and well studied in X-rays: (1) the warm absorbers in X-rays (WAX) sample, from Laha et al. (2014), which consists of 26 nearby ($z < 0.06$) Seyfert 1 galaxies, with an X-ray luminosity of $10^{42} < L_{2-10\ \rm keV} < 10^{45}$ erg s^{-1}; (2) "Palomar Green (PG) quasars," from Laor et al. (1994), which consists of quasars in a redshift range $z = 0.06 - 1.72$, with an X-ray luminosity of $10^{43} < L_{2-10\ \rm keV} < 10^{46}$ erg s^{-1}; (3) the WISSH quasar sample, from Martocchia et al. (2017), which consists of *WISE*-SDSS-selected high-redshift quasars ($z = 3 - 4$) with an X-ray luminosity of $10^{44} < L_{2-10\ \rm keV} < 10^{46}$ erg s^{-1}. and (4) the 12 μm selected AGN sample by Brightman & Nandra (2011), for which we have used a subsample of 10 sources that are type-1 AGNs having well-estimated values of $L_{2-10\ \rm keV}$ and $L_{\rm bol}$ (Vasudevan & Fabian 2009). The type-1 constraint on these IR-bright sources ensures that we obtain an unobscured view of the central engine. In the left panel of Figure 4 we have overplotted the bolometric correction ($L_{2-10\ \rm keV}/L_{\rm bol}$) versus $L_{\rm bol}$ of these comparison samples along with the MOX sample. We find that the X-ray bolometric corrections of most of the MOX sources are orders of magnitude lower than those of the Seyfert galaxies and the quasars. We also find that the *NuSTAR* estimates of the bolometric correction for the MOX sources (plotted as yellow triangles) are nearly similar to the Seyfert galaxies and quasars except for the source Mrk 231, which has a correction of $\log(L_{2-10\ \rm keV,\ X\text{-}ray\ spectra}/L_{\rm AGN}) = -3.62$. Therefore, it may be possible that most of the MOX sources are not X-ray weak, but instead heavily obscured.

The broad absorption line (BAL) quasars have also been found to be extremely X-ray weak. A study of two BAL quasars, PG 1004+130 (radio-loud) and PG 1700+518 (radio-quiet), by Luo et al. (2013), using *NuSTAR* data, has revealed that although they are among the optically brightest BAL

Table 3
Details of X-Ray Observations

Index	Source	Telescope	Observation ID	Observation Date	Exposure (ks)	Net Exposure (ks)	Total Counts
1	IRAS F08572+3915	*XMM-Newton*	0200630101	2004 Apr 13	29	14	2.28e+02
2	IRAS F10565+2448	*XMM-Newton*	0150320201	2003 Jun 17	32	25	1.307e+03
3	IRAS 23365+3604	*Chandra*	4115	2003 Feb 03	10	10	74
4	Mrk 273	*XMM-Newton*	0722610201	2013 Nov 04	23	6	9.81e+02
5	Mrk 876	*XMM-Newton*	0102040601	2002 Nov 14	13	0.1	3.06e+02
6	I Zw 1	*XMM-Newton*	0743050301	2015 Jan 19	141	20	1.81e+05
7	MrK 231	*XMM-Newton*	0770580501	2015 May 28	26	21	3.63e+03
8	NGC 1266	*XMM-Newton*	0693520101	2012 Jul 23	139	96	9.80e+03
9	M82	*XMM-Newton*	0206080101	2004 Apr 21	104	62	3.08e+05
10	NGC 1377	*Chandra*	16086	2013 Dec 10	48	44	2.06e+02
11	NGC 6240	*XMM-Newton*	0147420201	2003 Mar 14	42	4	2.61e+03
12	NGC 3256	*XMM-Newton*	0300430101	2005 Dec 06	134	97	5.54e+04
13	NGC 3628	*XMM-Newton*	0110980101	2000 Nov 27	65	38	6.29e+03
14	NGC 253	*XMM-Newton*	0152020101	2003 Jun 19	141	…	…
15	NGC 6764	*Chandra*	9269	2008 Jan 20	20	20	5.89e+02
16	NGC 1068	*XMM-Newton*	0740060201	2014 Jul 10	64	44	5.26e+05
17	IC 5063	*Chandra*	7878	2007 Jun 15	35	34	5.37e+03
18	NGC 2146	*XMM-Newton*	0110930101	2001 Aug 26	27	12	6.34e+03
19	IRAS 17208−0014	*XMM-Newton*	0081340601	2002 Feb 19	19	12	6.89e+02
20	NGC 1614	*Chandra*	15050	2012 Nov 21	16	16	8.33e+02
21	IRAS 05083+7936	*XMM-Newton*	009400101	2001 Sep 11	33	26	9.59e+02
22	IRAS 13451+1232	*Chandra*	836	2000 Feb 24	28	25	1.42e+03
23	3C 293	*Chandra*	12712	2010 Nov 16	69	68	2.12e+03
24	NGC 1433	*Chandra*	16345	2015 Mar 04	49	49	3.30e+02
25	IRAS 13120−5453	*XMM-Newton*	0693520201	2013 Feb 20	129	85	6.15e+03
26	IRAS 14378−3651	*Chandra*	7889	2007 Jun 25	14	14	1.05e+02
27	IRAS F11119+3257	*Chandra*	3137	2002 Jun 30	19	18	2.89e+03
28	IRAS F01572+0009	*XMM-Newton*	0101640201	2000 Jul 29	15	5	6.42e+03
29	IRAS F05024−1941	*XMM-Newton*	0405950401	2007 Feb 07	42	26	6.89e+02
30	IRAS F05189−2524	*XMM-Newton*	0722610101	2013 Oct Feb	38	30	1.48e+04
31	IRAS 07251−0248	*Chandra*	7804	2006 Dec Jan	16	15	7.80e+01
32	IRAS F07599+6508	*XMM-Newton*	0094400301	2001 Oct 24	23	16	7.12e+02
33	IRAS 09022−3615	*XMM-Newton*	0670300401	2012 Apr 23	33	16	1.16e+03
34	IRAS F09320+6134	*XMM-Newton*	0085640201	2001 Nov 12	35	26	1.49e+03
35	IRAS F12072−0444	*Chandra*	4109	2003 Feb Jan	10	10	7.3e+01
36	IRAS F12112+0305	*XMM-Newton*	0081340801	2001 Dec 30	23	18	4.92e+02
37	IRAS F14348−1447	*XMM-Newton*	0081341401	2002 Jul 29	22	15	7.97e+02
38	IRAS F14394+5332	*XMM-Newton*	0651100301	2015 Jul 06	13	8	3.31e+02
39	IRAS F15327+2340	*XMM-Newton*	0205510201	2005 Jan 14	35	6.3	5.09e+02
40	IRAS F15462−0450	*Chandra*	10348	2009 Apr 23	15	15	6.08e+02
41	IRAS F19297−0406	*Chandra*	7890	2007 Jun 18	17	…	…
42	IRAS 19542+1110	*Chandra*	7817	2007 Sep 10	15	15	4.27e+02
43	IRAS F20551−4250	*XMM-Newton*	0081340401	2001 Apr 21	22	11	1.07e+03
44	IRAS F23233+2817	*XMM-Newton*	0553870101	2008 Dec 15	80	52	2.07e+03
45	NGC 5506	*XMM-Newton*	0554170101	2009 Jan 02	90	61	7.94e+05
46	NGC 7479	*XMM-Newton*	0301651201	2005 Jun 24	16	0.57	9.8e+01
47	NGC 7172	*XMM-Newton*	0414580101	2007 Apr 24	58	28	9.81e+04

quasars, their 2–10 keV luminosity is 16–120 times weaker as compared to typical quasars. Another study by Luo et al. (2014) of six optically bright BAL quasars using *NuSTAR* and *Chandra* revealed that the 2 keV luminosities of the sources are almost >330 times fainter than those of normal Seyfert galaxies, while the overall hard X-ray 8–24 keV luminosity is consistently weak for all six sources. Extreme Compton-thick absorption ($N_{\rm H} > 10^{25}\,{\rm cm}^{-2}$) is ruled out from the analysis of the stacked *Chandra* spectra, confirming that the sources are bona fide X-ray weak. One possibility for the X-ray weakness of the BAL quasars is the failed winds, which are ionized clouds that do not get enough radiative push to get out of the gravitational field of the SMBH and fall back on the central engine. These failed winds obscure a substantial fraction of the AGN luminosity in the X-rays, making them X-ray weak. Another possibility is that the BAL outflows remove the feeding gas near the SMBH, thereby quenching the central AGN. The latter possibility can hold true for MOs. Observations by Cicone et al. (2014) have shown that MO kinetic energy can be as large as ∼5% of the AGN bolometric luminosity, which, according to feedback models (Hopkins & Elvis 2010), is enough to blow away the gases in the host galaxies. Martocchia et al. (2017) studied the X-ray properties of a sample of hyperluminous quasars ($L_{\rm bol} \geqslant 2 \times 10^{47}\,{\rm erg\,s}^{-1}$) at redshift of $z \sim 2 - 4$. They found that the X-ray bolometric correction for these sources lies in the range of $\sim 10^{-3}$–10^{-2},

Table 4
The X-Ray Properties of the Sources with MO

Index	Source	$\log F_{0.6-2\ \mathrm{keV}}$ erg cm^{-2} s^{-1}	$\log F_{2-10\ \mathrm{keV}}$ erg cm^{-2} s^{-1}	$\log L_{0.6-2\ \mathrm{keV}}$ erg s^{-1}	$\log L_{2-10\ \mathrm{keV}}$ erg s^{-1}	KT_1[a] APEC	KT_2[a] APEC	Γ	N_{H} (cm^{-2})	χ^2/dof
1	IRAS F08572+3915	...	...	...	...	...	...	...	...	...
2	IRAS F10565+2448	0	$-13.345^{+0.05}_{-0.05}$	0	41.25 ± 0.05	...	...	$2.17^{+0.23}_{-0.23}$	0	72/54 ∼ 1.54
3	IRAS 23365+3604	...	...	...	...	...	...	...	...	...
4	Mrk 273	-13.44 ± 0.05	$-12.35^{+0.05}_{-0.05}$	41.43 ± 0.04	42.25 ± 0.05	...	...	1.98 ± 0.32	$<10^{20}$	70/37 ∼ 1.90
5	Mrk 876	0	$-11.47^{+0.05}_{-0.05}$	0	44.11 ± 0.04	...	...	$2.04^{+0.17}_{0.18}$	0	14/11 ∼ 1.27
6	I Zw 1	-10.99 ± 0.01	$-11.21^{+0.005}_{-0.005}$	43.84 ± 0.01	43.63 ± 0.02	...	...	$2.37^{+0.08}_{-0.04}$	4.5×10^{20}	307/219 ∼ 1.41
7	MrK 231	-10.64 ± 0.02	$-12.14^{+0.05}_{-0.05}$	43.93 ± 0.02	42.42 ± 0.04	0.25 ± 0.10	0.80 ± 0.10	1.8[b]	$0.91^{+0.17}_{-0.17} \times 10^{22}$	181/117 ∼ 1.55
8	NGC 1266	-10.95 ± 0.01	$-13.15^{+0.04}_{-0.04}$	41.98 ± 0.01	39.78 ± 0.05	0.08 ± 0.02	0.16 ± 0.05	$1.79^{+0.3}_{-0.3}$	$0.78^{+0.02}_{-0.02} \times 10^{22}$	231/124 ∼ 1.87
9	M82	...	$-10.90^{+0.002}_{-0.002}$	...	40.32 ± 0.06	0.82 ± 0.12	...	$1.83^{+0.03}_{-0.03}$	$0.29^{+0.1}_{-0.1} \times 10^{22}$	818/239 ∼ 3.42
10	NGC 1377[1]	...	...	...	...	...	...	...	...	...
11	NGC 6240	-12.78 ± 0.05	$-11.80^{+0.03}_{-0.03}$	41.87 ± 0.02	42.28 ± 0.05	0.03 ± 0.01	...	$1.90^{+0.27}_{-0.27}$	0	149/77 ∼ 1.94
12	NGC 3256	-13.51 ± 0.02	$-12.35^{+0.01}_{-0.01}$	41.06 ± 0.02	40.97 ± 0.03	0.62 ± 0.22	1.10 ± 0.02	$2.40^{+0.06}_{-0.06}$	$0.24^{+0.02}_{-0.02} \times 10^{22}$	443/193 ∼ 2.32
13	NGC 3628	-20.30 ± 0.02	$-12.26^{+0.02}_{-0.02}$	0	40.22 ± 0.04	0.10 ± 0.02	...	$1.50^{+0.08}_{-0.08}$	$0.30^{+0.04}_{-0.04} \times 10^{22}$	172/154 ∼ 1.12
14	NGC 253	...	...	...	...	...	...	...	...	...
15	NGC 6764	-13.23 ± 0.04	$-13.19^{+0.06}_{-0.04}$	40.16 ± 0.04	39.85 ± 0.05	0.98 ± 0.05	...	>2.28	$0.25^{+0.21}_{-0.09} \times 10^{22}$	67/72 ∼ 0.93
16	NGC 1068	...	$-11.29^{+0.005}_{-0.005}$	...	40.95 ± 0.11	...	...	$1.92^{+0.2}_{-0.2}$	0	505/175 ∼ 2.88
17	IC 5063	-13.35 ± 0.03	$-10.79^{+0.02}_{-0.02}$	40.25 ± 0.03	42.57 ± 0.03	0.81 ± 0.14	<2.4	1.8[b]	$21.47^{+0.92}_{-0.92} \times 10^{22}$	612/490 ∼ 1.25
18	NGC 2146	-12.71 ± 0.03	$-12.00^{+0.02}_{-0.02}$	39.50 ± 0.03	40.20 ± 0.03	0.77 ± 0.15	...	$1.59^{+0.12}_{-0.10}$	$0.20^{+0.11}_{-0.11} \times 10^{22}$	329/119 ∼ 2.77
19	IRAS 17208−0014	-13.88 ± 0.15	$-12.98^{+0.2}_{-0.2}$	40.68 ± 0.17	41.59 ± 0.15	0.76 ± 0.23	...	1.8[b]	$6.23^{+18}_{-5} \times 10^{22}$	14/27
20	NGC 1614	-13.35 ± 0.20	$-12.86^{+0.03}_{-0.03}$	40.33 ± 0.20	40.82 ± 0.18	0.79 ± 0.13	...	1.8[b]	$0.24^{+0.24}_{-0.22} \times 10^{22}$	108/110 ∼ 0.98
21	IRAS 05083+7936	-13.98 ± 0.13	$-13.28^{+0.12}_{-0.02}$	40.79 ± 0.13	41.49 ± 0.11	0.75 ± 0.11	...	1.8[b]	$4.89^{+4.92}_{-3.52} \times 10^{22}$	79/38 ∼ 2.08
22	IRAS 13451+1232	-14.16 ± 0.08	$-11.89^{+0.02}_{-0.02}$	41.63 ± 0.08	43.64 ± 0.09	0.61 ± 0.17	...	$1.69^{+0.30}_{-0.20}$	$3.23^{+0.52}_{-0.52} \times 10^{22}$	182/230 ∼ 0.79
23	3C 293	-14.06 ± 0.03	$-11.78^{+0.01}_{-0.09}$	41.07 ± 0.03	42.85 ± 0.04	1.06 ± 0.29	<2.11	<1.4	$7.42^{+0.82}_{-0.82} \times 10^{22}$	262/320 ∼ 0.820
24	NGC 1433	-13.43 ± 0.07	$-13.32^{+0.09}_{-0.07}$	38.91 ± 0.07	39.02 ± 0.08	0.52 ± 0.10	...	1.8	0	44/51 ∼ 0.86
25	IRAS 13120−5453	-13.98 ± 0.02	$-12.76^{+0.03}_{-0.03}$	40.32 ± 0.02	41.54 ± 0.05	1.24 ± 0.1	...	$1.50^{+0.08}_{-0.15}$	$0.22^{+0.03}_{-0.07} \times 10^{22}$	223/146 ∼ 1.53
26	IRAS 14378−3651	...	...	...	...	...	...	...	...	
27	IRAS F11119+3257	-14.19 ± 0.05	$-11.79^{+0.01}_{-0.01}$	41.76 ± 0.05	44.16 ± 0.11	0.40 ± 0.15	...	$1.83^{+0.13}_{-0.13}$	$0.83^{+0.09}_{-0.09} \times 10^{22}$	282/280 ∼ 1.00
28	IRAS F01572+0009	-14.73 ± 0.20	$-12.07^{+0.02}_{-0.02}$	41.07 ± 0.21	43.73 ± 0.12	0.07 ± 0.02	...	$2.26^{+0.10}_{-0.10}$	$<0.009 \times 10^{22}$	103/85 ∼ 1.21
29	IRAS F05024−1941	-14.72 ± 0.20	$-13.46^{+0.3}_{-0.2}$	41.24 ± 0.21	42.50 ± 0.18	<2.16	...	1.8	0	25/25 ∼ 1.00
30	IRAS F05189−2524	-13.14 ± 0.02	$-11.25^{+0.005}_{-0.005}$	41.42 ± 0.02	43.31 ± 0.11	0.09 ± 0.02	...	$1.86^{+0.11}_{-0.10}$	$6.61^{+0.70}_{-0.70} \times 10^{22}$	286/209 ∼ 1.37
31	IRAS 07251−0248	...	...	...	...	...	...	...	...	...
32	IRAS F07599+6508	-13.90 ± 0.08	<−11.34	41.81 ± 0.08	43.37 ± 0.12	0.11 ± 0.02	0.75 ± 0.02	1.8[b]	0	17/27 ∼ 0.64
33	IRAS 09022−3615	-14.15 ± 0.45	$-12.70^{+0.09}_{-0.09}$	40.73 ± 0.45	42.19 ± 0.42	0.64 ± 0.32	...	1.8[b]	0	63/48 ∼ 1.32
34	IRAS F09320+6134	-13.53 ± 0.03	$-11.83^{+0.07}_{-0.07}$	40.97 ± 0.04	42.67 ± 0.05	0.85 ± 0.21	...	1.8[b]	0	82/62 ∼ 1.34
35	IRAS F12072−0444	-14.25 ± 0.03	$-13.05^{+0.4}_{-0.4}$	41.33 ± 0.20	42.53 ± 0.18	<0.99	...	1.8[b]	0	1.4/2 ∼ 0.71
36	IRAS F12112+0305	-14.69 ± 0.05	$-13.47^{+0.4}_{-0.4}$	40.39 ± 0.20	41.60	<0.68	...	1.8[b]	0	20/17 ∼ 1.19
37	IRAS F14348−1447	0	$-13.22^{+0.13}_{-0.11}$	0	41.96 ± 0.12	...	...	1.8[b]	0	32/32 ∼ 1.0
38	IRAS F14394+5332	0	$-13.41^{+0.1}_{-0.1}$	0	41.97 ± 0.11	...	...	1.8[b]	0	12/10 ∼ 1.2
39	IRAS F15327+2340	-13.40 ± 0.20	$-12.66^{+0.11}_{-0.20}$	40.67 ± 0.21	41.17 ± 0.15	0.73 ± 0.15	...	1.8[b]	0	38/18 ∼ 2.15
40	IRAS F15462−0450	-14.23 ± 0.22	$-12.38^{+0.05}_{-0.05}$	41.11 ± 0.26	42.97 ± 0.23	0.25 ± 0.14	...	1.8[b]	0	72/95 ∼ 0.77
41	IRAS 19297−0406	...	...	...	...	...	...	...		
42	IRAS 19542+1110	-14.03 ± 0.09	$-12.32^{+0.05}_{-0.05}$	40.90 ± 0.18	42.61 ± 0.14	>1.92	...	1.8[b]	0	68/61 ∼ 1.12
43	IRAS F20551−4250	-13.62 ± 0.18	$-12.99^{+0.15}_{-0.15}$	40.94 ± 0.18	41.57 ± 0.15	0.60 ± 0.25	...	1.8[b]	0	52/39 ∼ 1.34

Table 4
(Continued)

Index	Source	$\log F_{0.6-2\ \mathrm{keV}}$ erg cm^{-2} s^{-1}	$\log F_{2-10\ \mathrm{keV}}$ erg cm^{-2} s^{-1}	$\log L_{0.6-2\ \mathrm{keV}}$ erg s^{-1}	$\log L_{2-10\ \mathrm{keV}}$ erg s^{-1}	KT_1[a] APEC	KT_2[a] APEC	Γ	N_{H} (cm^{-2})	χ^2/dof
44	IRAS F23233+2817	-18.61 ± 0.05	$-13.95^{+0.05}_{-0.05}$	0	41.50 ± 0.15	<0.04	⋯	1.8[b]	0	$71/70 \sim 1.0$
45	NGC 5506	-12.12 ± 0.01	$-9.866^{+0.001}_{-0.001}$	40.86 ± 0.01	43.11 ± 0.05	⋯	⋯	$1.78^{+0.01}_{-0.01}$	$3.09^{+0.03}_{-0.03} \times 10^{22}$	$453/261 \sim 1.74$
46	NGC 7479	⋯	⋯	⋯	⋯	⋯	⋯	⋯	⋯	⋯
47	NGC 7172	-13.24 ± 0.03	$-10.16^{+0.01}_{-0.01}$	⋯	42.91 ± 0.06	0.75 ± 0.14	<2.5	$1.56^{+0.08}_{-0.04}$	$7.79^{+0.30}_{-0.20} \times 10^{22}$	$267/269 \sim 1.07$

Note.
[a] in units of keV.
[b] Sources for which the power-law slope Γ could not be constrained and hence fixed to $\Gamma = 1.8$.

Table 5
$L_{2-10\ \mathrm{keV}}$ Luminosity of the MOX Sources Obtained Using Different Methods and the Final List of Values Used in the Correlations

Index	Source	$\log L_{2-10\ \mathrm{keV}}$ (XMM/*Chandra*)[1] erg s^{-1}	$\log L_{2-10\ \mathrm{keV}}$ (*NuSTAR*)[2] erg s^{-1}	$\log L_{2-10\ \mathrm{keV}}$ Final Selection[5] erg s^{-1}
(1)	(2)	(3)	(4)	(5)
1	IRAS F08572+3915(CT)	41.38[a] (a)	⋯	43.38[b]
2	IRAS F10565+2448	41.25	⋯	41.25
3	IRAS 23365+3604	41.51[a] (b)	⋯	41.51
4	Mrk 273	42.25	42.93 (A)	42.93
5	Mrk 876	44.11	⋯	44.11
6	I Zw 1	43.62	⋯	43.62
7	MrK 231	42.42	42.47 (B)	42.47
8	NGC 1266	39.78	⋯	39.78
9	M82	40.32	⋯	40.32
10	NGC 1377(CT)	39.00[a] (c)	⋯	41.00[b]
11	NGC 6240(CT)	42.28	43.84 (C)	43.84
12	NGC 3256	40.96	40.04 (D)	40.96
13	NGC 3628	40.22	⋯	40.22
14	NGC 253	39.00[a] (d)	39.47 (E)	39.47
15	NGC 6764	39.85	⋯	39.85
16	NGC 1068(CT)	40.95	43.84 (F)	43.84
17	IC 5063	42.57	⋯	42.57
18	NGC 2146	40.20	⋯	40.20
19	IRAS 17208−0014	41.58	⋯	41.58
20	NGC 1614	40.82	⋯	40.82
21	IRAS 05083+7936	41.49	⋯	41.49
22	IRAS 13451+1232	43.64	⋯	43.64
23	3C 293	42.85	⋯	42.85
24	NGC 1433	39.01	⋯	39.01
25	IRAS 13120−5453(CT)	41.54	43.09 (G)	43.09
26	IRAS 14378−3651	41.53[a] (e)	⋯	41.96
27	IRAS F11119+3257	44.16	⋯	44.16
28	IRAS F01572+0009	43.73	⋯	43.73
29	IRAS F05024−1941	42.50	⋯	42.50
30	IRAS F05189−2524	43.31	43.56 (H)	43.56
31	IRAS 07251−0248	43.20[a] (f)	⋯	43.20
32	IRAS F07599+6508	43.37	42.70 (I)	43.37
33	IRAS 09022−3615	42.18	43.14 (J)	43.14
34	IRAS F09320+6134	42.67	⋯	42.67
35	IRAS F12072−0444	42.53	⋯	42.53
36	IRAS F12112+0305	41.60	⋯	41.60
37	IRAS F14348−1447(CT)	41.96	⋯	43.96[b]
38	IRAS F14394+5332	41.97	⋯	41.97
39	IRAS F15327+2340	41.16	⋯	41.16
40	IRAS F15462−0450	45.96	⋯	42.96
41	IRAS F19297−0406	41.25[a] (g)	⋯	41.25
42	IRAS 19542+1110	42.62	⋯	42.61
43	IRAS F20551−4250(CT)	41.57	⋯	43.57[b]
44	IRAS F23233+2817	41.50	⋯	41.50
45	NGC 5506	43.11	⋯	43.11
46	NGC 7479	42.00[a,c]	⋯	42.00
47	NGC 7172	42.90	⋯	42.90

Notes.
[a] The $L_{2-10\ \mathrm{keV}}$ of the MOX sources estimated using the hardness ratio method. Columns (1) and (2): source indices and names. Column (3): $L_{2-10\ \mathrm{keV}}$ values of the MOX sources obtained using X-ray spectral fits and the HR method using *XMM-Newton* and *Chandra* observations. References for the HR method: a = Teng & Veilleux (2010); b = Iwasawa et al. (2011); c = Aalto et al. (2016); d = Krips et al. (2016); e = Iwasawa et al. (2011); f = Nardini & Risaliti (2011); g = Iwasawa et al. (2011). Column (4): intrinsic $L_{2-10\ \mathrm{keV}}$ values obtained using *NuSTAR* observations. References for *NuSTAR* observations: A = Teng et al. (2015); B = Teng et al. (2014); Reynolds et al. (2017); C = Puccetti et al. (2016); D = Lehmer et al. (2015); E = Lehmer et al. (2013); F = Marinucci et al. (2016); G = Teng et al. (2015); H = Teng et al. (2015); I = Luo et al. (2014); J = Oda et al. (2017). Column (5): final set of $L_{2-10\ \mathrm{keV}}$ values of the MOX sources used in the correlations and analysis throughout this work.
[b] The C-thick sources for which we multiplied the $L_{2-10\ \mathrm{keV}}$ obtained in Column (3) by a factor of 100.
[c] This was obtained using broadband X-ray spectroscopy using *XMM-Newton* observations by Brightman & Nandra (2011).

Table 6
$L_{2-10\ \mathrm{keV}}$ of the MOX Sources Calculated Using Two Methods

Index	Source	log $L_{2-10\ \mathrm{keV}}$[a] ($L_{2-10\ \mathrm{keV,\ X\text{-}ray\ spectra}}$) (erg s^{-1})	log $L_{2-10\ \mathrm{keV}}$[b] 12 μm flux ($L_{2-10\ \mathrm{keV},\ 12\ \mu\mathrm{m}}$) (erg s^{-1})
1	IRAS F08572+3915	43.38	44.27
2	IRAS F10565+2448	41.25	42.71
3	IRAS 23365+3604	41.51	43.61
4	Mrk 273	42.93	43.48
5	Mrk 876	44.11	44.52
6	I Zw 1	43.62	44.76
7	MrK 231	42.47	44.76
8	NGC 1266	39.78	41.90
9	M82	40.32	40.24
10	NGC 1377	41.00	41.99
11	NGC 6240	43.84	43.81
12	NGC 3256	40.96	40.94
13	NGC 3628	40.22	40.19
14	NGC 253	39.47	⋯
15	NGC 6764	39.85	40.99
16	NGC 1068	43.84	42.95
17	IC 5063	42.57	43.46
18	NGC 2146	40.20	39.83
19	IRAS 17208−0014	41.58	42.70
20	NGC 1614	40.82	⋯
21	IRAS 05083+7936	41.49	⋯
22	IRAS 13451+1232	43.64	44.63
23	3C 293	42.85	⋯
24	NGC 1433	39.01	⋯
25	IRAS 13120−5453	43.09	43.55
26	IRAS 14378−3651	41.96	43.41
27	IRAS F11119+3257	44.16	45.08
28	IRAS F01572+0009	43.73	44.76
29	IRAS F05024−1941	42.50	44.31
30	IRAS F05189−2524	43.56	44.34
31	IRAS 07251−0248	43.20	43.63
32	IRAS F07599+6508	43.37	45.09
33	IRAS 09022−3615	43.14	43.99
34	IRAS F09320+6134	42.67	43.59
35	IRAS F12072−0444	42.53	44.57
36	IRAS F12112+0305	41.60	43.46
37	IRAS F14348−1447	43.96	43.54
38	IRAS F14394+5332	41.97	44.10
39	IRAS F15327+2340	41.16	42.43
40	IRAS F15462−0450	42.96	44.18
41	IRAS F19297−0406	41.25	43.64
42	IRAS 19542+1110	42.61	43.34
43	IRAS F20551−4250	43.57	43.84
44	IRAS F23233+2817	41.50	44.27
45	NGC 5506	43.11	43.22
46	NGC 7479	42.	43.11
47	NGC 7172	42.90	43.00

Notes.
[a] The 2–10 keV luminosity obtained in Column (7) of Table 5.
[b] The 2–10 keV luminosity obtained from the 12 μm flux as described in Section 2.3.

which are orders of magnitude lower than low-luminosity AGNs. They conjecture that possibly the X-ray weakness could be due to the powerful high-ionization emission-line-driven winds that perturb the X-ray corona and weaken their emission. On a similar vein, we find that although the MOX sources have a wide range of X-ray bolometric corrections, on an average they are mostly lower compared to the other quasar samples, and possibly the MOs are responsible for their lower X-ray bolometric corrections.

It is not very straightforward to understand why the AGNs at the center of the MOX galaxies can be X-ray weak, given the fact that the AGN bolometric luminosities of these galaxies are comparable to local Seyfert galaxies and quasars ($L_{\mathrm{AGN}} \sim 10^{41} - 10^{46}$ erg s^{-1}). The X-ray coronal emission is very unlikely to be affected by MOs because the AGN corona is confined to a location $\ll$ pc while the MOs are detected at distances of kiloparsec scales. Therefore, a direct link between the MOs and quenching of X-ray emission does not seem feasible. In light of this argument, we probe in detail the possibility of extreme Compton-thick obscuration of the MOX galaxies. In the scenario where the X-ray photons find it hard to escape out of the dust, the 12 μm flux gives us an approximate upper limit on the $L_{2-10\ \mathrm{keV}}$ luminosity (see Section 2.3). The right panel of Figure 4 shows the bolometric correction $\log(L_{2-10\ \mathrm{keV}}/L_{\mathrm{AGN}})$ versus the bolometric luminosity L_{AGN}, where the $L_{2-10\ \mathrm{keV}}$ values have been calculated using the 12 μm luminosity. We find that the range of the bolometric corrections calculated using 12 μm flux is similar to that of local Seyfert galaxies, and also the MOX galaxies follow the trend of having a lower bolometric correction for sources with higher bolometric luminosity, as also detected in Seyfert galaxies and quasars (see, e.g., Martocchia et al. 2017, and references therein). The $L_{2-10\ \mathrm{keV}}$ values estimated using 12 μm flux may therefore be good indicators of the intrinsic $L_{2-10\ \mathrm{keV}}$ luminosity, as it shows that the AGN central engine at the center of the MOX sources functions similarly to that of the Seyfert galaxies and quasars. From the right panel of Figure 3 we find that the ratio between the $L_{2-10\ \mathrm{keV}}$ of the MOX sources obtained using the 12 μm flux and that using X-ray spectroscopy ranges from 10^{-1} to 10^{3}, indicating that these estimates differ by orders of magnitude. The possible reasons behind this discrepancy could be any or all of the following: (1) the X-ray spectra do not give us the correct estimate of intrinsic X-ray luminosity owing to uncertainties in the obscuring column; (2) the 12 μm flux can contain emission from polycyclic aromatic hydrocarbons (PAHs) from the host galaxy (see, e.g., Hernán-Caballero et al. 2015, and the references therein), which mostly affects the mid-IR energy band; (3) the AGN emission factor α_{AGN} may have an intrinsic uncertainty leading to uncertainties in the estimates of $L_{2-10\ \mathrm{keV}}$. In a future work we intend to address these uncertainties with a more comprehensive multi-wavelength approach.

In summary, we find that on an average the AGNs at the centers of the MOX sources may not actually be X-ray weak. The apparent X-ray weakness could be due to the large obscuration column of the intervening dust and gas. The *NuSTAR* estimates and the 12 μm estimates of the bolometric corrections of the MOX sources mostly lie in the range spanned by Seyfert galaxies and quasars. Therefore, the AGNs at the heart of these galaxies may be functioning similarly to those of the local Seyfert galaxies and quasars, and the X-ray emission is weak owing to obscuration. As a caveat, we must remember that the $L_{2-10\ \mathrm{keV}}$ estimated using 12 μm flux is an indirect measurement and there can be other contributors to the 12 μm flux apart from the AGN and the SB processes, such as the PAH emission from galaxies.

Table 7
Total Bolometric Luminosity, AGN Luminosity, an X-Ray Bolometric Correction Fraction of the Sources

Index	Source	$\log L_{\rm bol}$ erg s^{-1}	$\alpha_{\rm AGN}$ (%)	$\log L_{\rm AGN}$	References for $\alpha_{\rm AGN}$	$\log(L_{2-10\ \rm keV,\ X\text{-}ray\ spectra}/L_{\rm AGN})$[a]	$\log(L_{2-10\ \rm keV,\ 12\ \mu m}/L_{\rm AGN})$[a]
1	IRAS F08572+3915	45.78	70.4	45.62	1	−2.24	−1.36
2	IRAS F10565+2448	45.68	47.1	45.35	1	−4.10	−2.64
3	IRAS 23365+3604	45.80	44.6	45.45	1	−3.93	−1.83
4	Mrk 273	45.79	34.2	45.32	1	−2.39	−1.84
5	Mrk 876	45.87	92.6	45.83	1	−1.72	−1.32
6	I Zw 1	45.59	90.1	45.54	1	−1.92	−0.97
7	MrK 231	46.18	80.5	46.08	1	−3.62	−1.32
8	NGC 1266	43.91	25	43.30	2	−3.52	−1.40
9	M82	44.58	0.09	41.53	2	−1.21	−1.29
10	NGC 1377	43.63	20	42.93	2	−1.93	−0.94
11	NGC 6240	45.48	78	45.37	1	−1.53	−1.56
12	NGC 3256	45.12	0.07	41.96	2	−1.00	−1.02
13	NGC 3628	43.83	0.09	40.78	2	−0.56	−0.59
14	NGC 253	44.06	0.04	40.66	2	…	…
15	NGC 6764	43.99	1.7	42.22	2	−2.37	−1.23
16	NGC 1068	44.95	9.7	43.94	2	−0.09	−0.98
17	IC 5063	44.34	90	44.29	2	−1.72	−0.83
18	NGC 2146	44.61	0.03	41.08	2	−0.88	−1.25
19	IRAS 17208−0014	46.08	5	44.77	1	−3.19	−2.07
20	NGC 1614	45.34	0	0	4	…	…
21	IRAS 05083+7936	45.63	0	0	1	…	…
22	IRAS 13451+1232	45.96	80.6	45.87	1	−2.23	−1.26
23	3C 293	…	…	…	…	…	…
24	NGC 1433	…	…	…	…	…	…
25	IRAS 13120−5453	45.88	33.4	45.40	1	−2.31	−1.85
26	IRAS 14378−3651	45.75	21.1	45.07	1	−3.11	−1.66
27	IRAS F11119+3257	46.29	80	46.19	1	−2.03	−1.11
28	IRAS F01572+0009	46.26	64.6	46.07	1	−2.34	−1.31
29	IRAS F05024−1941	46.01	7.3	44.87	1	−2.37	−0.56
30	IRAS F05189−2524	45.80	71.7	45.65	1	−2.09	−1.31
31	IRAS 07251−0248	46.03	30.0	45.51	1	−2.30	−1.87
32	IRAS F07599+6508	46.17	87.6	46.11	1	−2.74	−1.02
33	IRAS 09022−3615	45.93	54.9	45.66	1	−2.53	−1.67
34	IRAS F09320+6134	45.63	56.4	45.38	1	−2.71	−1.79
35	IRAS F12072−0444	46.04	74.8	45.91	1	−3.38	−1.34
36	IRAS F12112+0305	45.96	17.8	45.21	1	−3.61	−1.75
37	IRAS F14348−1447	45.98	17.4	45.22	1	−1.26	−2.68
38	IRAS F14394+5332	45.75	62.5	45.54	1	−3.57	−1.44
39	IRAS F15327+2340	45.80	5.8	44.56	1	−3.40	−2.13
40	IRAS F15462−0450	45.85	60.6	45.63	1	−2.67	−1.45
41	IRAS F19297−0406	46.02	23.4	45.38	1	−4.13	−1.74
42	IRAS 19542+1110	45.70	25.5	45.11	1	−2.49	−1.76
43	IRAS F20551−4250	45.69	56.9	45.44	1	−1.87	−1.60
44	IRAS F23233+2817	45.69	44.6	45.33	1	−3.84	−1.06
45	NGC 5506	44.21	93.3	44.18	3	−1.06	−0.95
46	NGC 7479	43.49	83.7	43.41	3	−1.41	−0.30
47	NGC 7172	44.37	92.4	44.33	3	−1.44	−1.33

Notes.
[a] See Section 4.1 for the definition of $L_{2-10\ \rm keV,\ X\text{-}ray\ spectra}$ and $L_{2-10\ \rm keV,\ 12\ \mu m}$.
References: (1) Veilleux et al. (2013); (2) Cicone et al. (2014); (3) Stone et al. (2016); (4) Armus et al. (2009).

6.2. Is the AGN the Main Driver of Molecular Outflows?

The left panel of Figure 5 shows the correlation between the $L_{2-10\ \rm keV}$ and MO velocity in the MOX sample, while the right panel shows the correlation between $L_{2-10\ \rm keV}$ and MO mass outflow rate. The correlations are statistically significant (see Table 8), and the positive slope indicates that a stronger AGN emission drives faster and more powerful MOs. We find that the correlations between $L_{2-10\ \rm keV}$ and MO dynamical quantities become stronger when we use the $L_{2-10\ \rm keV}$ estimated using 12 μm flux (see Figure 6). Figure 7 shows that the MO outflow velocity and the mass outflow rates correlate very strongly with the AGN bolometric luminosity. In the left panel of Figure 7 we find that two SB-dominated sources Arp 220 and IRAS F12112+0305 have larger AGN luminosity, $L_{\rm AGN}$, compared to other SB galaxies, although their AGN fraction is small, 5.8% and 17.8%, respectively (see Table 7). However, the MO velocities in those sources are $\leqslant$400 km s^{-1}, comparable to the other SB galaxies. From the right panel of Figure 7

Table 8
Correlation Results between Parameters x and y ($y = ax + b$)

Correlation	a	Dev(a)	b	Dev(b)	R_S	P_{null}	Data Points
$L_{2-10\ keV}$ versus MO vel	150	18	−5901	766	0.56	4×10^{-5}	47
$L_{2-10\ keV}$ versus MO $\dot{M}_{out}$	0.55	0.07	−21	2.89	0.76	1.1×10^{-5}	25
$L_{2-10\ keV,\ 12\ \mu m}$ versus MO vel	180	24	−7382	1063	0.70	2.6×10^{-7}	43
$L_{2-10\ keV,\ 12\ \mu m}$ versus MO $\dot{M}_{out}$	0.51	0.06	−19	2.40	0.81	3.8×10^{-6}	22
$L_{0.6-2\ keV}$ versus MO vel	173	37	−6686	1520	0.59	4×10^{-4}	31
$L_{0.6-2\ keV}$ versus MO $\dot{M}_{out}$	0.52	0.08	−19.58	3.31	0.83	2.5×10^{-5}	17
L_{AGN} versus MO vel	155	18	−6511	813	0.70	1.48×10^{-7}	43
L_{AGN} versus MO $\dot{M}_{out}$	0.45	0.04	−17.93	1.93	0.86	3.8×10^{-7}	25
$L_{Starburst}$ versus MO vel	197	61	−8437	2775	0.40	0.008	43
$L_{Starburst}$ versus MO $\dot{M}_{out}$	1.02	0.16	−43.99	7.22	0.57	0.005	22

we find a tight correlation between the L_{AGN} and the MO mass outflow rate with a probability >99.99%. A recent study by Fiore et al. (2017) found similar strong correlations not only between the MOs and L_{AGN} but also with ionized outflows and L_{AGN}. The linear regression slope derived by them for $\log(L_{AGN})$ versus $\log(\dot{M}_{out})$ is 0.76 ± 0.06 for molecular winds. We find a flatter slope of 0.45 ± 0.04, probably as a result of the fact that the SB-dominated galaxies skew the correlation. We note from Figures 5–7 that the SB-dominated sources (in green circles) have the lowest MO velocity and $\dot{M}_{out}$. These results indicate that the central AGN plays a dominant role in driving these large-scale MOs.

Sturm et al. (2011) in a sample of six galaxies detected MOs and found that the MO velocity scales positively with the strength of the AGN. They concluded that the central AGN plays a definitive role in driving these large-scale outflows. Moreover, the authors predicted that we can distinguish between an AGN-driven MO and an SB-driven one by noting the velocity of the outflow. Typically AGN-driven flows are faster, ∼1000 km s^{-1}, while the SB-driven outflows are slower, 200–400 km s^{-1}. More recent studies by Cicone et al. (2014) on a sample of 19 sources with MOs show that the molecular mass outflow rates increase with the strength of the central AGN. The SB-dominated sources, on the other hand, harbor outflows with lower mass outflow rates. These point to the fact that the central AGN plays a dominant role in driving these outflows.

Although we find that the presence of an AGN boosts the MO velocity and $\dot{M}_{out}$, the physical nature of the interaction between the central AGN and the MO is still not clear. One possibility investigated by previous studies is the effect of highly ionized high-velocity outflows (UFOs) striking the ISM. Feruglio et al. (2015) detected the presence of UFOs and MOs in the galaxy Mrk 231. The MO extends to 1 kpc, which the authors conjectured could be driven by the UFOs by transferring the kinetic energy to the ISM. Tombesi et al. (2015) found similar trends of energy-conserving interactions of the faster UFOs and the slower MO for the source IRAS F11119+3257, suggesting that the UFOs could be the mechanism generating large MOs at kiloparsec scales. This theory is, however, still debated (Veilleux et al. 2017). Moreover, except for two MOX sources, Mrk 231 and IRAS F11119+3257, no other sources exhibit simultaneous detections of MOs and UFOs, which can also be due to low S/N in the spectral range of 7–9 keV where the UFOs are found. Another mechanism that may produce large-scale MOs is the radiative thrust from the central AGN, very similar to UV line-driven disk winds (Proga & Kallman 2004). The presence of dust enhances the possibility of coupling the AGN radiation with the interstellar matter and thereby transferring the radiative thrust onto the gas leading to the MO. However, it is not clear how the AGN emission from < pc radial distance influences molecular gas clouds at kiloparsec scales and what physical mechanism tranfers momentum and energy efficiently in the region parsecs to kiloparsecs from the host galaxy.

The question therefore remains, is the presence of an AGN necessary to generate and drive an MO? Geach et al. (2014) have detected MOs in a compact massive SB galaxy at a redshift of ∼0.7 that are mainly driven by stellar radiation pressure. The authors demonstrated that nuclear bursts of star formation can eject large amounts of cold gas from the center of the galaxies, which truncates the star formation and affects their evolution. Similarly, Sell et al. (2014) in a sample of 12 massive galaxies, at $z \sim 0.6$, exhibiting signs of rapid quenching of star formation rate, have shown that the quenching is happening likely as a result of feedback from the fast outflows generated by star formation rather than AGNs. For 9/12 galaxies the authors rule out the presence of any AGN at the center of the galaxies. Diamond-Stanic et al. (2012) in a sample of SB galaxies at $z \sim 0.6$ also find that radiation pressure from massive stars and ram pressure from supernova and stellar winds are sufficient to produce high-velocity outflows, and the presence of an AGN is not needed in such cases. Theoretical studies by Sharma & Nath (2013) have also suggested that SBs can play an active role in driving massive galactic winds.

From Table 7 we find that more than 50% (27 out of 47) of the sources in the MOX sample have an AGN fraction of <50%, implying that the total galactic emission is dominated by SBs in more than half of the sources. Very interestingly, we also find statistically significant positive correlations between the soft X-ray APEC luminosity $L_{0.6-2\ keV}$ (APEC) and MO velocity and $\dot{M}_{out}$. In this work we assume that APEC luminosity in the energy range of 0.6–2 keV probes the strength of SB activity. As a caveat, we note that this may not be true for a few sources where the primary or the reflected emission from AGNs may also contribute to the 0.6–2 keV luminosity. We also find statistically strong positive correlations between $L_{Starburst}$ versus MO velocity and $L_{Starburst}$ versus $\dot{M}_{out}$ (see Figure 9). These correlations indicate that SB also can play a significant role in generating and driving the MOs. The SB emission arises from extended regions of the galaxies (compared to the size of the central AGN) and is sometimes cospatial with the MO (∼ kpc) and hence has a good

probability to generate the MO. However, we should note that the correlations of the MO velocity and $\dot{M}_{\rm out}$ with the $L_{\rm Starburst}$ and $L_{0.6-2{\rm keV}}$ are weaker compared to those of the AGN X-ray and bolometric luminosities. It is possible that both SBs and AGNs generate and drive these massive MO.

In summary we confirm that the AGN power is well correlated with the power of the MO. However, the fact that the powerful MOs are also found in sources whose contribution to the AGN bolometric luminosity is small, as well as the strong correlations between $L_{0.6-2{\rm keV}}$ versus $\dot{M}_{\rm out}$ and $L_{\rm Starburst}$ versus $\dot{M}_{\rm out}$, indicates that powerful SBs are equally probable to generate and drive the large-scale MOs.

7. Conclusions

We have carried out an extensive X-ray spectral analysis of a sample of 47 galaxies exhibiting MOs (the MOX sample), using observations from *Chandra* and *XMM-Newton*. Below we list the main conclusions:

1. From the X-ray spectra of the MOX sources we find that they are generally X-ray weak, with an X-ray bolometric correction ranging from $L_{2-10\ {\rm keV}}/L_{\rm AGN} \sim 10^{-4.5}$ to $10^{-0.5}$, with 70% of the sources below 10^{-2}. Possibly the MOX sources have AGNs with weaker X-ray emission compared to local Seyfert galaxies and quasars. However, it is not physically clear why and how should the X-ray emission be selectively quenched relative to the overall AGN bolometric luminosity.
2. We obtain an upper limit on the $L_{2-10\,{\rm keV}}$ emission from the AGN ($L_{2-10\ {\rm keV},\ 12\,\mu{\rm m}}$) in the MOX sources using the 12 μm flux emitted from the galaxies, following the correlation by Asmus et al., $\log\left(\frac{L_{2-10\ {\rm keV}}}{10^{43}\ {\rm erg\ s^{-1}}}\right) = -0.32 + 0.95 \times \log\left(\frac{L_{12\,\mu{\rm m}} \times \alpha_{\rm AGN}}{10^{43}\ {\rm erg\ s^{-1}}}\right)$. The factor $\alpha_{\rm AGN}$ ensures that we consider the 12 μm flux from the central AGN only. The $L_{2-10\ {\rm keV},\ 12\,\mu{\rm m}}$ values obtained using this method are 0.5–3 orders of magnitude larger than the $L_{2-10\,{\rm keV}}$ values obtained using X-ray spectroscopy. Moreover, the $L_{2-10\ {\rm keV},\ 12\,\mu{\rm m}}$ values are consistent with local Seyfert galaxies and quasars. Speculatively, we can say that the AGNs at the heart of the MOX sources may have similar $L_{2-10\,{\rm keV}}$ to local Seyfert galaxies and quasars, but their weak X-ray emission is due to the high column of obscuration along the line of sight. As a caveat, we must note that the galactic PAH emission also contributes to the 12 μm flux, which is unaccounted for, and hence we refer to the $L_{2-10\ {\rm keV},\ 12\,\mu{\rm m}}$ obtained using the 12 μm flux as an upper limit on the 2–10 keV emission from the AGN.
3. The relation ($L_{2-10\ {\rm keV},\ 12\,\mu{\rm m}}/L_{\rm AGN}$) versus $L_{\rm AGN}$ of the MOX sources also shows a similar trend to that of the local Seyfert galaxies and quasars, that is, with increasing bolometric luminosity of AGNs ($L_{\rm AGN}$) the X-ray bolometric correction decreases. This may imply that at the heart of these galaxies the AGN functions similarly to that of the quasars, and their apparent X-ray weakness is due to extreme obscuration.
4. We find statistically significant positive correlations between $L_{2-10\,{\rm keV}}$ and $L_{\rm AGN}$ with the MO velocity and $\dot{M}_{\rm out}$ in the MOX sample, indicating that the presence of an AGN boosts the MO velocity and power.
5. We find that the SB emission in the host galaxies of the MOX sample, $L_{\rm Starburst}$, correlates strongly with the MO velocity and $\dot{M}_{\rm out}$. The SB emission, measured in the soft X-rays (0.6–2 keV) with the model APEC, also shows significant correlation with the MO velocity and $\dot{M}_{\rm out}$. These correlations points to the fact that the SB has the potential to generate and drive the MOs. The SB emission arises from regions that are more extended (compared to the size of the AGN central engine) and hence may sometimes be cospatial with the MOs, and therefore it can play a more important role in driving the outflows. Supporting our claim above, we also find that 27 of the 47 sources in the MOX sample have an AGN fraction $<50\%$, implying that the SBs are dominant in these galaxies and can drive these large-scale MOs. However, we should note that the correlations of the MO velocity and $\dot{M}_{\rm out}$ with the $L_{\rm Starburst}$ and $L_{0.6-2{\rm keV}}$ are weaker compared to those of the AGN X-ray and bolometric luminosities. It is possible that although SBs can drive massive MOs, the presence of an AGN always boosts the power of the outflows.

S.L. is grateful to Silvia Martocchia for supplying the X-ray bolometric corrections and AGN bolometric luminosities for the PG quasars and the high-redshift bright quasar sample (WISSH). S.L. is also grateful to Daniel Stern, Sylvain Veilleux, Richard Mushotzky, and Richard Rothschild for sharing interesting ideas involved in this work. This research has made use of the NASA/IPAC Extragalactic Database (NED), which is operated by the Jet Propulsion Laboratory, California Institute of Technology, under contract with the National Aeronautics and Space Administration.

Appendix A
The Best-fit Spectra and Models

In this section we show the best-fit data for the sources in the MOX sample, along with the best-fit model and the residuals after the data have been fitted with the model. For sources with counts $\leqslant$200 we have shown the spectra for viewing purposes only, as we have used the HR method to calculate the luminosity.

Appendix B
Description of the Individual Sources in the MOX Sample

1. IRAS F08572+3915: This is a double-nucleus ULIRG. The source has been identified as Compton thick (Teng & Veilleux 2010), and the previous studies have estimated an absorption column density of $\sim 10^{25}$ cm^{-2}. The power-law photon index $\Gamma = -0.43$ is not constrained owing to low counts. The authors classified this as a weak ULIRG. This source has also been studied by Iwasawa et al. (2011) using *Chandra* observations. The source luminosities estimated by the authors are $L_{\rm SX} = 8.0 \times 10^{40}$ erg s^{-1} and $L_{\rm HX} = 2.0 \times 10^{41}$ erg s^{-1} in the soft and hard bands, respectively. *NuSTAR* hard X-ray studies were carried out by Teng et al. (2015), and the authors conclude that the source is X-ray weak and could not be detected in any of the *NuSTAR* energy bands. The MOs in this source have been detected using the IRAM-PDBI telescope with the CO (1–0) emission line (Cicone et al. 2014).

In our analysis, we found that this source has very low counts, and hence the HR method was used to calculate the 2–10 keV luminosity.

2. IRAS F10565+2448: This is a pair of interacting spiral galaxies and is a heavily obscured source. Teng & Veilleux (2010) studied this source using *Chandra* observations and have estimated an absorption column density of $0.05^{+0.07}_{-0.04} \times 10^{22}\,\mathrm{cm}^{-2}$, implying a Compton-thin obscurer. The estimated power law $\Gamma = 1.62^{+0.14}_{-0.13}$. Iwasawa et al. (2011) studied the *Chandra* observation of this source and have estimated a luminosity of $L_{\mathrm{SX}} = 1.21 \times 10^{41}\,\mathrm{erg\,s^{-1}}$ and $L_{\mathrm{HX}} = 1.6 \times 10^{41}\,\mathrm{erg\,s^{-1}}$. The authors mention that the hard X-ray emission is point-like but the soft X-ray emission is much more extended up to 7″. *NuSTAR* hard X-ray studies carried out by Teng et al. (2015) could not detect the source in any energy band of *NuSTAR*.

   We could not constrain the intrinsic neutral absorption for this source. The best-fit photon index is $\Gamma = 2.17^{+0.23}_{-0.23}$. In addition, we required an absorption edge at 0.34 keV.

3. IRAS 23365+3604: Iwasawa et al. (2011) studied the *Chandra* data of this source and found that it is a heavily obscured source. A faint X-ray source is present in the nucleus, which, however, could not be studied properly because of the short exposure of the observation (∼10 ks). The hard X-ray color HR = −0.22 points to the fact that this object is an AGN, which is Compton thick. This source was also studied by Teng et al. (2005), who found $\Gamma = 1.10^{+0.35}_{-0.25}$ and an absorption column density of $50^{+39}_{-27} \times 10^{20}\,\mathrm{cm}^{-2}$.

   Due to lack of counts, the HR method was used to calculate the 2–10 keV luminosity.

4. Mrk 273: Classified as Seyfert 2 (NED). Hernández-García et al. (2015) classified the candidate as a changing-look candidate with both Compton-thick and Compton-thin signatures available from different observations. *NuSTAR* hard X-ray studies were carried out by Teng et al. (2015), and an intrinsic luminosity of $L_{2-10\ \mathrm{keV}} = 8.55 \times 10^{42}\,\mathrm{erg\,s^{-1}}$ was derived.

   In our study, we detected a broad Fe K line that was modeled by the *diskline* profile. Soft X-ray emission lines were modeled using a Gaussian profile. We could not detect any neutral absorption intrinsic to the source. The power-law slope $\Gamma < 1.58$ is very flat.

5. Mrk 876: This is a Seyfert 1 galaxy and has a strong AGN at its center. Early studies by Erkens et al. (1995) confirm that the source is variable in X-rays and UV. The *Swift*/XRT data studied by Bottacini et al. (2015) found a broad Fe Kα emission line. The Fe K line was also studied by de La Calle Pérez et al. (2010) using *XMM-Newton* data. Piconcelli et al. (2005) had studied this source as a part of a sample of PG quasars and reported $L_{2-10} = 1.78 \times 10^{44}\,\mathrm{erg\,s^{-1}}$.

   In our work, with the data quality being poor, we could not constrain any intrinsic neutral absorption. The spectra just required an absorbed power law, and the slope could be constrained. We derived similar X-ray luminosity to those of Piconcelli et al. (2005). The *NuSTAR* observation of this source is not yet made public.

6. I Zw 1: This is a narrow-line Sy1 galaxy and is highly variable. An extensive X-ray study of this source has been done by Gallo et al. (2007), and Piconcelli et al. (2005) studied the source as a part of a sample of PG quasars.

   For this source we detected two components of warm absorbers. There was also the presence of a broad Fe K emission line and a neutral intrinsic absorption column.

7. Mrk 231: Obscured source with a strong AGN, studied by Teng & Veilleux (2010). A connection between MOs and UFOs is found in this source by Feruglio et al. (2015). The authors confirm an energy-conserving mechanism responsible for creating the MOs from the UFOs. *Chandra* imaging and spectroscopy have been carried out by Veilleux et al. (2014). A *NuSTAR* hard X-ray view of this source has been carried out by Teng et al. (2015). A separate study using *NuSTAR* data focusing only on this source has been carried out by Teng et al. (2014), and the authors measured an X-ray luminosity of $L_{2-10\ \mathrm{keV}} = 3.94 \times 10^{42}\,\mathrm{erg\,s^{-1}}$. The authors concluded that this source is a Compton-thin AGN.

   We found that this source has a complex spectrum that required one component of warm absorber, one component of thermal emission (APEC), a neutral intrinsic absorption, and a broad Fe K emission line. The power-law slope is flat, and its lower value is pegged at $\Gamma = 1.5$.

8. NGC 1266: A nearby lenticular galaxy, harboring an AGN that powers a massive MO detected in this source that harbors an AGN (Alatalo et al. 2015). Apart from extensive analysis of *Chandra* and *XMM-Newton* data, a multiwaveband study was carried out by the authors, where they detected a soft emission from the SB and a power law and Fe K line from the AGN. The intrinsic absorption column density estimated for this source from IR studies of Alatalo et al. (2015) is $N_{\mathrm{H}} = 3 \times 10^{24}\,\mathrm{cm}^{-2}$, almost 3 orders of magnitude higher than that found using X-ray studies. Suppression of star formation in this SB galaxy is studied by Alatalo et al. (2015). There is a *NuSTAR* observation of this source, but there is no published study.

   In our study we found that this source has a complex spectrum that required a soft thermal component (APEC) along with a warm absorber, a neutral intrinsic absorber, and soft X-ray emission lines at 1.48 and 1.85 keV in the observer's frame. The Fe K line was not detected owing to poor S/N.

9. M82: This is an SB-dominated galaxy. Liu et al. (2014) studied the nuclear region of the source with 500 ks *Chandra* data. The Fe K α line is detected, and most of the hard X-ray emission 2–8 keV has a thermal origin. A weakly broadened Fe K line was detected by Caballero-García (2011).

   The spectrum is complex with several discrete emission features in the soft X-ray band. We could not obtain a good statistical fit to the data with the baseline models used in this work. We detected narrow Fe K emission. A neutral intrinsic absorber has also been detected.

10. NGC 1377: *Chandra* and *Swift* data are not published; hence, there are no previous studies available for this

source. With the source photon counts being weak, the HR method was used in our work.

11. NGC 6240: Mostly Compton-thick galaxy merger. Puccetti et al. (2016) studied the source with *NuSTAR* data and concluded that this source could be an early merger stage galaxy with two nuclei separated and an intrinsic source luminosity of $L_{2-10\ \mathrm{keV}} = 7 \times 10^{43}$ erg s^{-1}. Both active and obscured Compton-thick material is present. Wang et al. (2014) detected fast shock-heated gas within 5 kpc of the central region. Nardini et al. (2013) and Feruglio et al. (2013) have studied the *Chandra* data and detected a soft X-ray halo and also CO emission lines. Teng & Veilleux (2010) and Iwasawa et al. (2011) have studied the source in a sample. Netzer et al. (2005) have studied *XMM-Newton* observations of this source and found that SB emission dominates the soft X-ray 0.5–3 keV energy range.

    In our study the X-ray spectra required a broad Fe K emission line, along with a soft X-ray emission line at 0.89 keV. We could not constrain the intrinsic neutral absorption.

12. NGC 3256: Powerful SB galaxy studied by Lehmer et al. (2015) with *Chandra* and *NuSTAR* data. The nature of X-ray emission is unclear, as no obvious AGN signature was found. This galaxy was studied by Jenkins et al. (2004) and was referred to as an SB merger galaxy, and a hard X-ray bolometric correction was estimated to be $\sim 10^{-5}$. The $L_{2-10\ \mathrm{keV}} \sim 10^{40}$ erg s^{-1} has been estimated mostly from the ULXs and crowded X-ray sources, and not an AGN.

    In our study we found that the X-ray spectrum is complex. It required two thermal components in the soft X-rays (APEC), one neutral intrinsic absorber, and three Gaussian emission lines for three Fe K emission lines at different ionization states.

13. NGC 3628: Tsai et al. (2012) studied this SB galaxy and found a connection between MOs and emission-line plasma in X-rays. A study of the source was carried out by Strickland et al. (2001) using *Chandra* data, where they find a luminous X-ray source 20″ away from the nucleus.

    The spectrum required one thermal component (APEC), neutral intrinsic absorption, and a high-energy absorption in the Fe K band that was modeled using an inverted Gaussian. The power-law slope is pegged at $\Gamma = 1.5$.

14. NGC 253: A highly variable SB galaxy studied by *NuSTAR* (Lehmer et al. 2013). *NuSTAR* and *Chandra* data reveal that the nuclear region contains three bright X-ray point sources that are ULXs and not an AGN, and highly obscured with a column density of $\log N_{\mathrm{H}} = 23\ \mathrm{cm}^{-2}$. The Fe K line complex was studied by Mitsuishi et al. (2011), who found several highly ionized Fe K emission lines.

    Due to low photon counts, the HR method was employed in our work.

15. NGC 6764: This is an AGN + SB galaxy, and the *Chandra* data are studied by Croston et al. (2008).

    The hard X-ray band >2 keV has very few counts; hence, the power-law slope upper limit could not be constrained, $\Gamma > 2.28$. The soft X-ray emission was modeled using APEC.

16. NGC 1068: Compton-thick Sy2 galaxy studied by *NuSTAR* data by Bauer et al. (2015). Multicomponent X-ray reflectors were needed to fit the data. Kallman et al. (2014) studied the source with *Chandra* data and found that the amount of mass of gas necessary for the emission in X-rays is $\sim 3.7 \times 10^5\ M_{\odot}$. Shu et al. (2011) studied the Fe K line emission of the source. Marinucci et al. (2016) studied the source using *NuSTAR* data unveiling the obscured source.

    This source could not be modeled with the baseline model. The spectra show a very unique broad Fe K emission line, typical of Compton-thick objects.

17. IC 5063: Classified as narrow-line Sy2 radio galaxies, and the *Suzaku* data are studied by Tazaki et al. (2011). There are *NuSTAR* data, but they are not published. Marinucci et al. (2012) also studied the source in a sample of Sy2 sources that have exhibited a broad Fe K line in reflected spectra. The source is classified as Compton thin by Marinucci et al. (2012).

    It is an absorbed source with a concave spectra in the hard X-rays and diffuse soft X-ray emission. An absorbed power law and a blackbody for the diffuse soft X-ray emission could fit the data. There could be X-ray contribution from radio jets.

18. NGC 2146: The *Chandra* observation of this SB galaxy was carried out by Inui et al. (2005). There were six ultraluminous point sources detected in the field of view.

    In our work we found that the spectra can be modeled by an absorbed power law only.

19. IRAS 17208−0014: Teng & Veilleux (2010) and Iwasawa et al. (2011) have studied this source. This is a luminous ULIRG.

    In our work the power-law slope could not be constrained owing to low photon counts.

20. NGC 1614: ULIRG, and a star-forming galaxy studied in the multiwaveband by Herrero-Illana et al. (2014). This is also detected as a merger remnant by Saito et al. (2017) using ALMA data. The nature of the dominant emitting mechanism at the center is still under debate; however, AGN presence may not be needed to describe the spectral properties. Possibly a compact SB ($r \leqslant 90$ pc) is present. The total IR luminosity is $L = 4 \times 10^{11} L_{\odot}$ (Armus et al. 2009; Herrero-Illana et al. 2014). An upper limit to AGN luminosity is given by the authors, $L_{\mathrm{AGN}} \leqslant 4.5 \times 10^{11} L_{\odot}$.

    In our study, the power-law slope could not be constrained owing to low photon counts.

21. IRAS 05083+7936: This is an absorbed quasar. Ballo et al. (2014) had studied this absorbed quasar. *NuSTAR* hard X-ray studies were carried out by Teng et al. (2015).

    In our work, the power-law slope could not be constrained owing to low photon counts.

22. IRAS 13451+1232: A Seyfert 2 galaxy. Jia et al. (2013), Teng & Veilleux (2010), and LaMassa et al. (2014) studied the source in X-rays.

    We found that the hard X-ray photon count is poor; however, the power-law slope and the absorption column could be constrained.

23. 3C 293: Lanz et al. (2015) studied the jet–ISM interaction of this radio-loud source and stated how the molecular gas is heated by the jets. Only *Chandra* data are available for this source.

24. NGC 1433: Only *Chandra* data available, which are not published.

    In our study we found that the source has very poor data counts. The power-law slope and the intrinsic neutral absorption column density were frozen to a value of 1.5

and 0.07 $\times$ 10^{22} cm^{-2}, respectively, as they could not be constrained.

25. IRAS 13120−5453: 129 ks *XMM-Newton* data are not published yet. *NuSTAR* hard X-ray studies were carried out by Teng et al. (2015), who confirm it as a Compton-thick AGN.

    We found that this source has a narrow Fe K emission line.
26. IRAS 14378−3651: *NuSTAR* hard X-ray studies carried out by Teng et al. (2015), and the authors do not detect any source X-ray flux beyond 10 keV. The *Chandra* spectra have been studied by Iwasawa et al. (2011).
27. IRAS F11119+3257: Studied by Tombesi et al. (2015), who found strong MOs in IR using *Herschel*-PACS, as well as ultrafast outflows in the X-rays using the *Suzaku* telescope. Tombesi et al. (2017) observed this source with *NuSTAR* and detected a similar observed flux to ours.

    We found that this is a bright source and could be modeled with a simple absorbed power law and a very weak blackbody for the soft emission.
28. IRAS F01572+0009: This source is also known as Mrk 1014 (alias PG 0157+001). It has been studied by Ricci et al. (2014), and a 2–10 keV luminosity of $10^{43.80}$ erg s^{-1} has been estimated using the same data set used by us. The authors have detected reflection from distant matter and used the model *Mytorus*.

    We found that this is a low count source that could be modeled with a simple absorbed power law and a blackbody for the soft emission. The data did not require a neutral intrinsic absorber.
29. IRAS F05024−1941: This is a ULIRG and was studied by Teng & Veilleux (2010), and the authors have used the HR method to calculate the flux.

    The source has very low photon counts. The power-law slope and the neutral absorber $N_{\rm H}$ could not be constrained.
30. IRAS F05189−2524: A ULIRG studied by Teng & Veilleux (2010), and the authors found $L_{2-10\ \rm keV}$ = 2.3 $\times$ 10^{43} erg s^{-1}.

    The soft emission was modeled using two blackbody components. The spectra required two Gaussian emission lines for two Fe K complexes. The spectra are concave, indicating neutral absorption.
31. IRAS 07251−0248: This source is a ULIRG and has been studied by Iwasawa et al. (2011) and by Teng & Veilleux (2010), both of whom found the source to be a Compton-thin AGN. However, the source could not be detected in the X-rays (*Chandra*) by the authors (as well as by us) owing to its weakness and obscuration. The X-ray flux of the source estimated from the infrared analysis is $F_{2-10\ \rm keV}$ = 7.4 $\times$ 10^{-12} erg cm^{-2} s^{-1} (Nardini & Risaliti 2011).
32. IRAS F07599+6508: This is a Compton-thin absorbed ULIRG. Teng & Veilleux (2010) studied this source and calculated a luminosity of $L_{2-10\ \rm keV}$ = 1.12 $\times$ 10^{42} erg s^{-1} using the HR method. Imanishi & Terashima (2004) studied a sample of four ULIRGs with detectable broad near-infrared emission lines produced by AGNs, one of the sources being IRAS F07599+6508. Using spectral analysis, they could constrain the luminosity of the AGN $L_{2-10\ \rm keV}$ = 8 $\times$ 10^{41} erg s^{-1}.

    Very low photon counts did not allow us to constrain the power-law slope or the $N_{\rm H}$ of the intrinsic absorber.
33. IRAS 09022−3615: This is a LIRG, and Iwasawa et al. (2011) calculated an X-ray luminosity of $L_{2-10\ \rm keV}$ = 2.0 $\times$ 10^{42} erg s^{-1}. The authors found that the hard X-ray source is marginally resolved.

    Very low photon counts did not allow us to constrain the power-law slope or the $N_{\rm H}$ of the intrinsic absorber.
34. IRAS F09320+6134: The alternative name of this source is UGC 05101 and was studied in a large sample of ULIRGs by U et al. (2012). The authors have also estimated the infrared luminosity for all the sources. The X-ray flux estimated is $F_{2-10\ \rm keV}$ = 8.64 $\times$ 10^{-9} erg cm^{-2} s^{-1}, which is higher than our estimate of $10^{-11.83}$ erg cm^{-2} s^{-1}.

    Very low photon counts did not allow us to constrain the power-law slope or the $N_{\rm H}$ of the intrinsic absorber.
35. IRAS F12072−0444: This is a ULIRG and was studied by Teng & Veilleux (2010), who have calculated a luminosity of $L_{2-10\ \rm keV}$ = 1.5 $\times$ 10^{41} erg s^{-1}. Very low photon counts did not allow us to constrain the power-law slope or the $N_{\rm H}$ of the intrinsic absorber.
36. IRAS F12112+0305: This is a ULIRG and was studied by Teng & Veilleux (2010) and Iwasawa et al. (2011), who have calculated a luminosity of $L_{2-10\ \rm keV}$ = 1.5 $\times$ 10^{41} erg s^{-1} and 4 $\times$ 10^{41} erg s^{-1}, respectively.

    Very low photon counts did not allow us to constrain the power-law slope or the $N_{\rm H}$ of the intrinsic absorber.
37. IRAS F14348−1447: This is a ULIRG studied by Teng & Veilleux (2010), who estimated a luminosity of $L_{2-10\ \rm keV}$ = 7.4 $\times$ 10^{41} erg s^{-1}. Very low photon counts did not allow us to constrain the power-law slope or the $N_{\rm H}$ of the intrinsic absorber.
38. IRAS F14394+5332: This source has not been studied before.

    Very low photon counts did not allow us to constrain the power-law slope or the $N_{\rm H}$ of the intrinsic absorber.
39. IRAS F15327+2340: This source is also known as ARP 220 and is an SB galaxy. LaMassa et al. (2012) have worked on a sample of sources including this source where the authors have attempted to disentangle the AGN and SB contribution of the sources in the 0.5–2 keV soft X-ray band. It was also studied by Teng & Veilleux (2010), and they calculated a luminosity of $L_{2-10\ \rm keV}$ = 1.2 $\times$ 10^{41} erg s^{-1}.

    Very low photon counts did not allow us to constrain the power-law slope or the $N_{\rm H}$ of the intrinsic absorber.
40. IRAS F15462−0450: ULIRG studied by Teng & Veilleux (2010), and they calculated a luminosity of $L_{2-10\ \rm keV}$ = 1.3 $\times$ 10^{43} erg s^{-1} using the HR method.

    Very low photon counts did not allow us to constrain the power-law slope or the $N_{\rm H}$ of the intrinsic absorber.
41. IRAS 19297−0406: This source is a very faint source in X-rays and studied as a part of C-goals by Iwasawa et al. (2011), who calculated an X-ray luminosity of $L_{2-10\ \rm keV}$ = 1.8 $\times$ 10^{41} erg s^{-1} using the HR method.

    No significant counts. Hence, we used previous studies to estimate the X-ray luminosity.
42. IRAS 19542+1110: This source is a very faint source in X-rays and studied as a part of C-goals by Iwasawa et al. (2011), who calculated an X-ray luminosity of $L_{2-10\ \rm keV}$ = 1.0 $\times$ 10^{42} erg s^{-1} using the HR method.

    Very low photon counts did not allow us to constrain the power-law slope or the $N_{\rm H}$ of the intrinsic absorber.

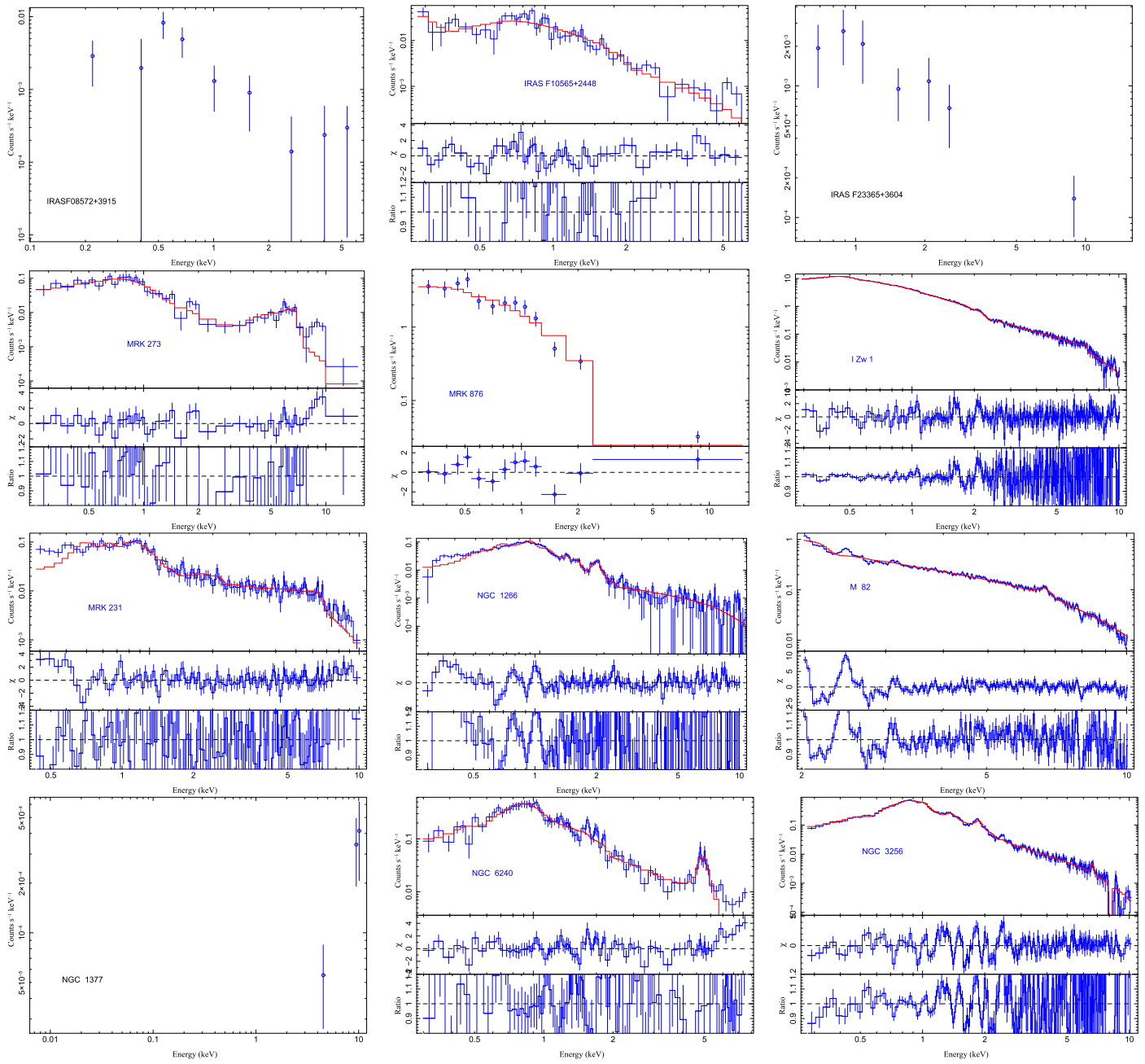

Figure 10. X-ray data, best-fit model, and residuals of the sources. For the sources where the low counts do not allow us to carry out standard fitting, we have plotted just the X-ray data. See Section 4 for details.

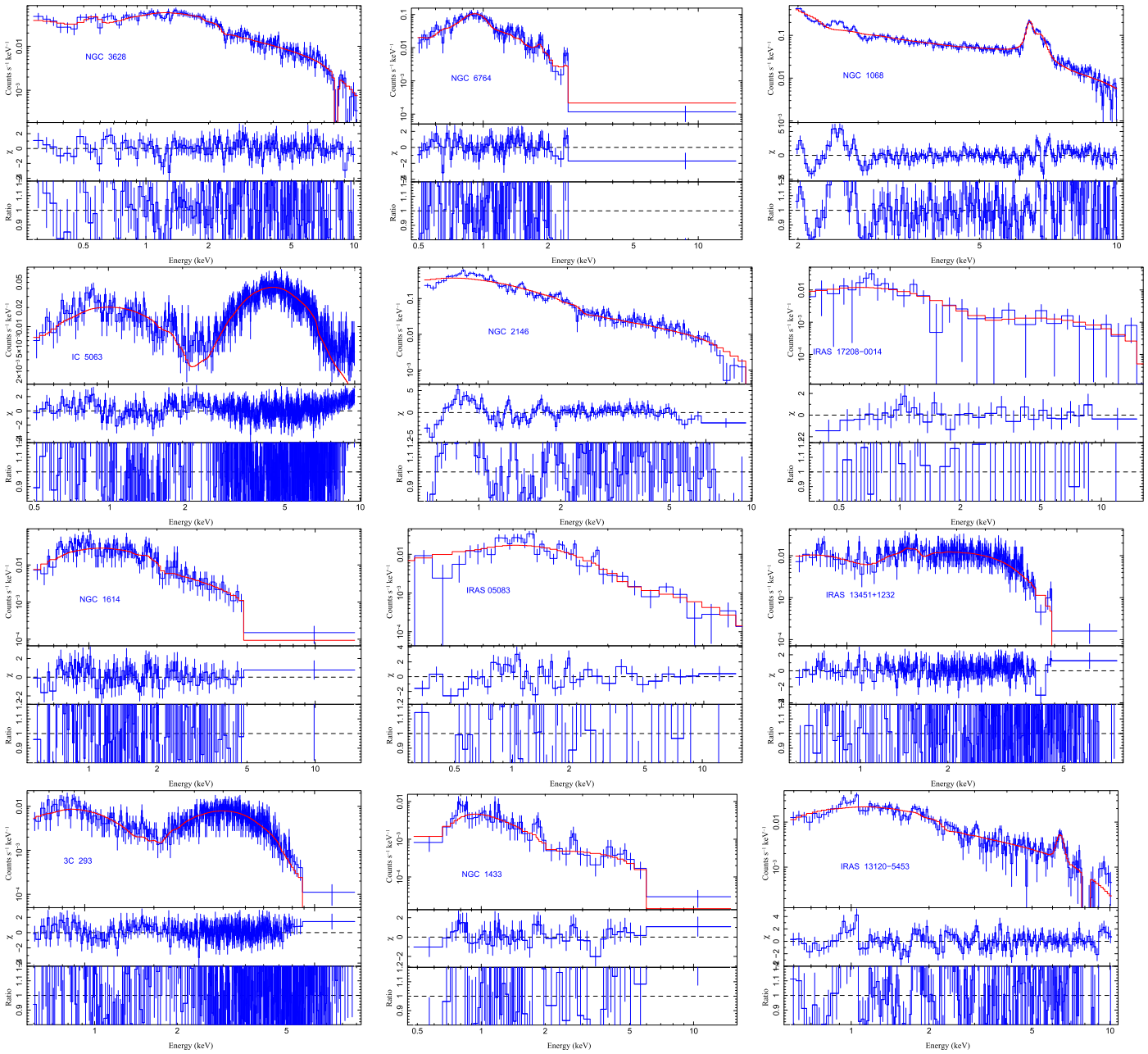

Figure 10. (Continued.)

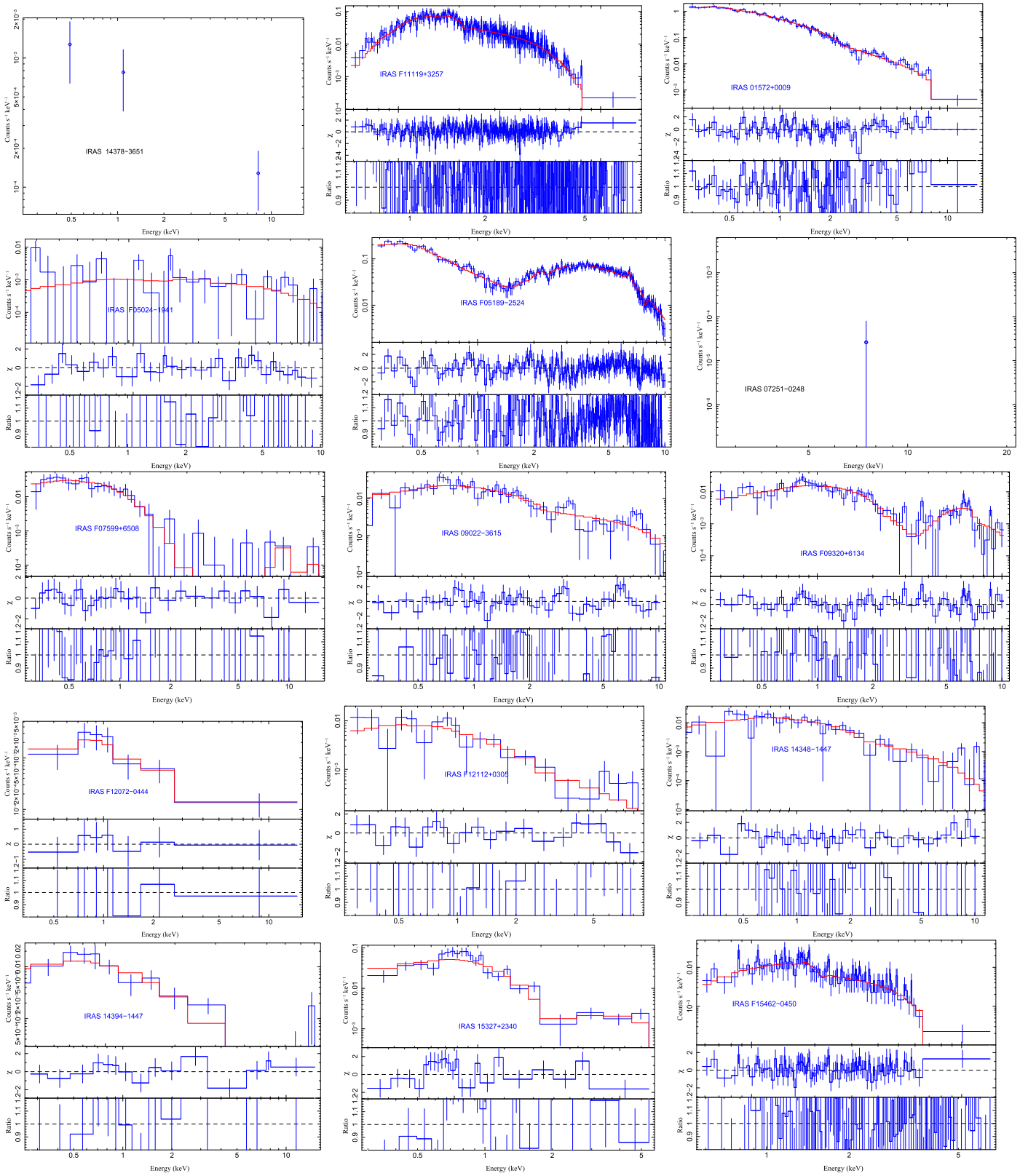

Figure 10. (Continued.)

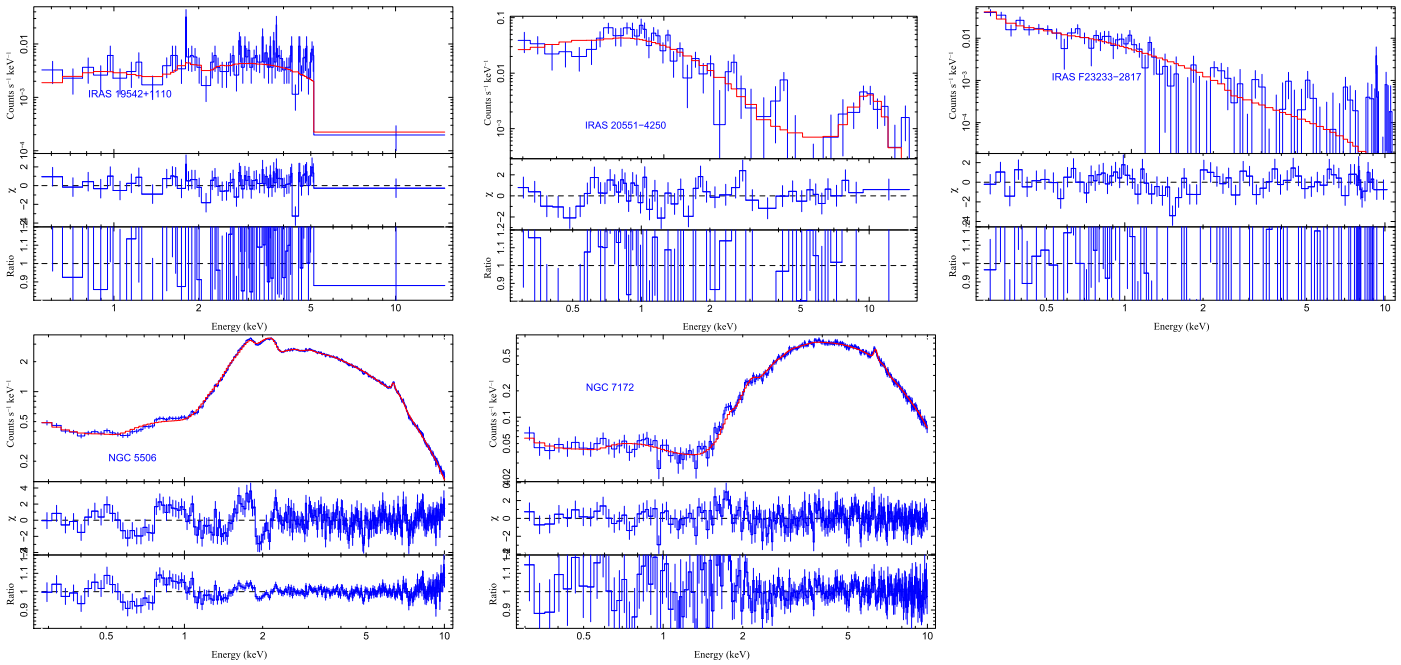

Figure 10. (Continued.)

43. IRAS F20551−4250: Also known as ESO 286-IG19 and studied by Iwasawa et al. (2011), who calculated an X-ray luminosity of $L_{2-10\ \mathrm{keV}} = 2.1 \times 10^{41}$ erg s^{-1}.

    Very low photon counts did not allow us to constrain the power-law slope or the N_{H} of the intrinsic absorber.
44. IRAS F22491−1808: Both Iwasawa et al. (2011) and Teng & Veilleux (2010) discuss this source, and the luminosities calculated by them are 0.6×10^{41} and 2.1×10^{41} erg s^{-1}, respectively.

    Very low photon counts did not allow us to constrain the power-law slope or the N_{H} of the intrinsic absorber.
45. NGC 5506: Guainazzi et al. (2010) studied the source, which is an X-ray-obscured Seyfert galaxy with a broad Fe Kα emission line. The maximum value of the luminosity quoted for this source is $L_{2-10\ \mathrm{keV}} = 1.1 \times 10^{43}$ erg s^{-1}. The source is an obscured Seyfert 1 galaxy.
46. NGC 7479: Akylas & Georgantopoulos (2009) studied the source in a sample of Sy1, Sy2, and Compton-thick galaxies, where they infer an X-ray luminosity of $L_{2-10\ \mathrm{keV}} = 2.8 \times 10^{40}$ erg s^{-1}. The source is a Seyfert 2 galaxy with significant obscuration.

    No significant counts. Hence, we used previous studies to estimate the X-ray luminosity.
47. NGC 7172: Guainazzi et al. (1998) studied this Seyfert 2 source and calculated a luminosity of $L_{2-10\ \mathrm{keV}} = 1.5 \times 10^{43}$ erg s^{-1}. The source is an obscured Seyfert 1 galaxy.

Appendix C
Sources in MOX Sample without *NuSTAR* Observations, as on 2017 December

In this section we list the 23 sources in the MOX sample that have not been observed by *NuSTAR*. The sources are IRAS 23365+3604, I Zw 1, NGC 1377, NGC 3628, NGC 2146, NGC 6764, IRAS 17208−0014, NGC 1614, IRAS 05083+7936, IRAS 13451+1232, 3C 293, NGC 1433, IRAS F01572+0009, IRAS F05024−1941, IRAS 07251−0248, IRAS 09022−3615, IRAS F12112+0305, IRAS F14348−1447, IRAS F14394+5332, IRAS F15462−0450, IRAS F19297−0406, IRAS 19542+1110, and IRAS F23233+2817.

ORCID iDs

Sibasish Laha https://orcid.org/0000-0003-2714-0487
Matteo Guainazzi https://orcid.org/0000-0002-1094-3147
Enrico Piconcelli https://orcid.org/0000-0001-9095-2782
Poshak Gandhi https://orcid.org/0000-0003-3105-2615
Claudio Ricci https://orcid.org/0000-0001-5231-2645
Ritesh Ghosh https://orcid.org/0000-0003-4790-2653
Alex G. Markowitz https://orcid.org/0000-0002-2173-0673
Joydeep Bagchi https://orcid.org/0000-0001-7466-1272

References

Aalto, S., Costagliola, F., Muller, S., et al. 2016, A&A, 590, A73
Aalto, S., Muller, S., Sakamoto, K., Gallagher, J. S., Martín, S., & Costagliola, F. 2012, A&A, 546, A68
Akritas, M. G., & Bershady, M. A. 1996, ApJ, 470, 706
Akylas, A., & Georgantopoulos, I. 2009, A&A, 500, 999
Alatalo, K., Blitz, L., Young, L. M., & Davis, T. A. 2011, ApJ, 735, 88
Alatalo, K., Lacy, M., Lanz, L., et al. 2015, ApJ, 798, 31
Asmus, D., Gandhi, P., Hönig, S. F., Smette, A., & Duschl, W. J. 2015, MNRAS, 454, 766
Armus, L., Mazzarella, J. M., Evans, A. S., Surace, J. A., & Sanders, D. B. 2009, PASP, 121, 559
Ballo, L., Severgnini, P., Della Ceca, R., et al. 2014, MNRAS, 444, 2580
Bauer, F. E., Arevalo, P., Walton, D. J., & Koss, M. J. 2015, ApJ, 812, 116
Bottacini, E., Orlando, E., Greiner, J., et al. 2015, ApJL, 798, L14
Brightman, M., & Nandra, K. 2011, MNRAS, 413, 1206
Brusa, M., Cresci, G., Daddi, E., et al. 2018, A&A, 612, A29
Brusa, M., Feruglio, C., Cresci, G., et al. 2015, A&A, 578, A11
Caballero-García, M. D. 2011, MNRAS, 418, 1973
Cicone, C., Maiolino, R., Sturm, E., et al. 2014, A&A, 562, A21
Combes, F., García-Burillo, S., Casasola, V., et al. 2013, A&A, 558, A124
Costagliola, F., Herrero-Illana, R., Lohfink, A., et al. 2016, A&A, 594, A114
Croston, J. H., Hardcastle, M. J., Kharb, P., Kraft, R. P., & Hota, A. 2008, ApJ, 688, 190

Dasyra, K. M., Combes, F., Novak, G. S., et al. 2014, A&A, 565, A46
de La Calle Pérez, I., Longinotti, A. L., Guainazzi, M., et al. 2010, A&A, 524, A50
Diamond-Stanic, A. M., Moustakas, J., Tremonti, C. A., et al. 2012, ApJL, 755, L26
Ducci, L., Sasaki, M., Haberl, F., & Pietsch, W. 2013, A&A, 553, A7
Elvis, M., Wilkes, B. J., McDowell, J. C., et al. 1994, ApJS, 95, 1
Erkens, U., Wagner, S. J., Alloin, D., et al. 1995, A&A, 296, 90
Fabian, A. C. 2012, ARA&A, 50, 455
Faucher-Giguère, C.-A., & Quataert, E. 2012, MNRAS, 425, 605
Ferrarese, L., & Merritt, D. 2000, ApJL, 539, L9
Feruglio, C., Fiore, F., Carniani, S., et al. 2015, A&A, 583, A99
Feruglio, C., Fiore, F., Maiolino, R., et al. 2013, A&A, 549, A51
Fiore, F., Feruglio, C., Shankar, F., et al. 2017, A&A, 601, A143
Gallo, L. C., Brandt, W. N., Costantini, E., et al. 2007, MNRAS, 377, 391
Gandhi, P., Horst, H., Smette, A., et al. 2009, A&A, 502, 457
García-Burillo, S., Combes, F., Usero, A., et al. 2015, A&A, 580, A35
Geach, J. E., Hickox, R. C., Diamond-Stanic, A. M., et al. 2014, Natur, 516, 68
Gebhardt, K., Bender, R., Bower, G., et al. 2000, ApJL, 539, L13
Guainazzi, M., Bianchi, S., Matt, G., et al. 2010, MNRAS, 406, 2013
Guainazzi, M., Matt, G., Antonelli, L. A., et al. 1998, MNRAS, 298, 824
Hernán-Caballero, A., Alonso-Herrero, A., Hatziminaoglou, E., et al. 2015, ApJ, 803, 109
Hernández-García, L., Masegosa, J., González-Martín, O., & Márquez, I. 2015, A&A, 579, A90
Herrero-Illana, R., Perez-Torres, M. Á, & Alonso-Herrero, A. 2014, ApJ, 786, 156
Hopkins, P. F., & Elvis, M. 2010, MNRAS, 401, 7
Houck, J. C., & Denicola, L. A. 2000, in ASP Conf. Ser. 216, Astronomical Data Analysis Software and Systems IX, ed. N. Manset, C. Veillet, & D. Crabtree (San Francisco, CA: ASP), 591
Imanishi, M., & Terashima, Y. 2004, AJ, 127, 758
Inui, T., Matsumoto, H., Tsuru, T. G., et al. 2005, PASJ, 57, 135
Iwasawa, K., Sanders, D. B., Teng, S. H., et al. 2011, A&A, 529, A106
Jenkins, L. P., Roberts, T. P., Ward, M. J., & Zezas, A. 2004, MNRAS, 352, 1335
Jia, J., Ptak, A., Heckman, T., & Zakamska, N. L. 2013, ApJ, 777, 27
Kalberla, P. M. W., Burton, W. B., Hartmann, D., et al. 2005, A&A, 440, 775
Kallman, T., Evans, D. A., Marshall, H., et al. 2014, ApJ, 780, 121
Krips, M., Martín, S., Sakamoto, K., & Aalto, S. 2016, A&A, 592, L3
Labiano, A., García-Burillo, S., Combes, F., et al. 2014, A&A, 564, A128
Laha, S., Guainazzi, M., Dewangan, G. C., Chakravorty, S., & Kembhavi, A. K. 2014, MNRAS, 441, 2613
LaMassa, S. M., Heckman, T. M., & Ptak, A. 2012, ApJ, 758, 82
LaMassa, S. M., Yaqoob, T., Ptak, A. F., et al. 2014, ApJ, 787, 61
Lamastra, A., Bianchi, S., Matt, G., et al. 2009, A&A, 504, 73
Lampton, M., Margon, B., & Bowyer, S. 1976, ApJ, 208, 177
Lanz, L., Ogle, P. M., Evans, D., et al. 2015, ApJ, 801, 17
Laor, A., Fiore, F., Elvis, M., Wilkes, B. J., & McDowell, J. C. 1994, ApJ, 435, 611
Lehmer, B. D., Tyler, J. B., Hornschemeier, A. E., et al. 2015, ApJ, 806, 126
Lehmer, B. D., Wik, D. R., Hornschemeier, A. E., et al. 2013, ApJ, 771, 134
Leroy, A. K., Walter, F., Decarli, R., et al. 2015, ApJ, 811, 15
Liu, J., Gou, L., Yuan, W., & Mao, S. 2014, MNRAS, 437, L76
Luo, B., Brandt, W. N., Alexander, D. M., Harrison, F. A., & Stern, D. 2013, ApJ, 772, 153
Luo, B., Brandt, W. N., Alexander, D. M., & Stern, D. 2014, ApJ, 794, 70
Maiolino, R., Ruiz, M., Rieke, G. H., & Papadopoulos, P. 1997, ApJ, 485, 552
Marinucci, A., Bianchi, S., Matt, G., et al. 2016, MNRAS, 456, L94
Marinucci, A., Bianchi, S., Nicastro, F., Matt, G., & Goulding, A. D. 2012, ApJ, 748, 130
Martocchia, S., Piconcelli, E., Zappacosta, L., et al. 2017, A&A, 608, A51
Mauersberger, R., Henkel, C., Wielebinski, R., Wiklind, T., & Reuter, H.-P. 1996, A&A, 305, 421
Mitsuishi, I., Yamasaki, N. Y., & Takei, Y. 2011, ApJL, 742, L31
Mitsuishi, I., Yamasaki, N. Y., & Takei, Y. 2013, PASJ, 65, 44
Nardini, E., & Risaliti, G. 2011, MNRAS, 415, 619
Nardini, E., Wang, J., Fabbiano, G., et al. 2013, ApJ, 765, 141
Nemmen, R. S., Georganopoulos, M., Guiriec, S., et al. 2012, Sci, 338, 1445
Netzer, H., Lemze, D., Kaspi, S., et al. 2005, ApJ, 629, 739
Oda, S., Tanimoto, A., Ueda, Y., et al. 2017, ApJ, 835, 179
Piconcelli, E., Jimenez-Bailón, E., Guainazzi, M., et al. 2005, A&A, 432, 15
Proga, D., & Kallman, T. R. 2004, ApJ, 616, 688
Puccetti, S., Comastri, A., Bauer, F. E., et al. 2016, A&A, 585, A157
Reynolds, C., Punsly, B., Miniutti, G., O'Dea, C. P., & Hurley-Walker, N. 2017, ApJ, 836, 155
Ricci, C., Bauer, F. E., Treister, E., et al. 2017, MNRAS, 468, 1273
Ricci, C., Ueda, Y., Ichikawa, K., et al. 2014, A&A, 567, A142
Saito, T., Iono, D., Xu, C. K., et al. 2017, ApJ, 835, 174
Sakamoto, K., Ho, P. T. P., & Peck, A. B. 2006, ApJ, 644, 862
Sanders, D. B., & Mirabel, I. F. 1985, ApJL, 298, L31
Sanders, D. B., Soifer, B. T., Elias, J. H., et al. 1988, ApJ, 325, 74
Sell, P. H., Tremonti, C. A., Hickox, R. C., et al. 2014, MNRAS, 441, 3417
Sharma, M., & Nath, B. B. 2013, ApJ, 763, 17
Shu, X. W., Yaqoob, T., & Wang, J. X. 2011, ApJ, 738, 147
Smith, R. K., Brickhouse, N. S., Liedahl, D. A., & Raymond, J. C. 2001, ApJL, 556, L91
Stone, M., Veilleux, S., Meléndez, M., et al. 2016, ApJ, 826, 111
Strickland, D. K., Colbert, E. J. M., Heckman, T. M., et al. 2001, ApJ, 560, 707
Sturm, E., González-Alfonso, E., Veilleux, S., et al. 2011, ApJL, 733, L16
Tazaki, F., Ueda, Y., Terashima, Y., & Mushotzky, R. F. 2011, ApJ, 738, 70
Teng, S. H., Brandt, W. N., & Harrison, F. A. 2014, ApJ, 785, 19
Teng, S. H., Rigby, J. R., Stern, D., et al. 2015, ApJ, 814, 56
Teng, S. H., & Veilleux, S. 2010, ApJ, 725, 1848
Teng, S. H., Wilson, A. S., Veilleux, S., et al. 2005, ApJ, 633, 664
Tombesi, F., Meléndez, M., Veilleux, S., et al. 2015, Natur, 519, 436
Tombesi, F., Veilleux, S., Meléndez, M., et al. 2017, ApJ, 850, 151
Tsai, A.-L., Matsushita, S., Kong, A. K. H., Matsumoto, H., & Kohno, K. 2012, ApJ, 752, 38
Tsai, C.-W., Turner, J. L., Beck, S. C., et al. 2006, AJ, 132, 2383
U, V, Sanders, D. B., Mazzarella, J. M., & Evans, A. S. 2012, ApJS, 203, 9
Vasudevan, R. V., & Fabian, A. C. 2009, MNRAS, 392, 1124
Vasudevan, R. V., Fabian, A. C., Gandhi, P., Winter, L. M., & Mushotzky, R. F. 2010, MNRAS, 402, 1081
Vasudevan, R. V., Mushotzky, R. F., Winter, L. M., & Fabian, A. C. 2009, MNRAS, 399, 1553
Veilleux, S., Bolatto, A., Tombesi, F., et al. 2017, ApJ, 843, 18
Veilleux, S., Melendez, M., Sturm, E., & Gracia-Carpio, J. 2013, ApJ, 776, 27
Veilleux, S., Teng, S. H., Rupke, D. S. N., Maiolino, R., & Sturm, E. 2014, ApJ, 790, 116
Walter, F., Weiss, A., & Scoville, N. 2002, ApJL, 580, L21
Wang, J., Nardini, E., Fabbiano, G., et al. 2014, ApJ, 781, 55
Wiklind, T., Combes, F., & Henkel, C. 1995, A&A, 297, 643
Zubovas, K., & King, A. 2012, ApJL, 745, L34